Aus dem Neurowissenschaftlichen Forschungszentrum
der Medizinischen Fakultät Charité – Universitätsmedizin Berlin

DISSERTATION

The role of medial entorhinal cortex layer three pyramidal cells in slow oscillations and spatial coding

zur Erlangung des akademischen Grades
Doctor of Philosophy (PhD)

vorgelegt der Medizinischen Fakultät
Charité – Universitätsmedizin Berlin

von
Mary Constance Clare Holman
aus Charlottetown, Kanada

Datum der Promotion: 26.06.2022

Contents

1. Abstract

In the decades since the first studies of amnesia in patient H.M., and subsequent discoveries of functional cell types linked to navigation, the hippocampus (HC) and medial entorhinal cortex (MEC) have been at the center of research on learning and memory. Activity of these structures is coordinated via neuronal oscillations, synchronizing the network at various frequencies including slow oscillations (< 1 Hz), theta (6 -11 Hz), gamma (40 -100 Hz) and ripple (140 – 200 Hz) oscillations. Layer 3 pyramidal cells (L3PCs) of the MEC send projections to area CA1 of the hippocampus, and are thought to be important for HC-MEC communication.

I sought to understand the role of L3PCs of the MEC in two types of network activity. First, using optogenetic tools, I silenced L3PCs in an anaesthetized model of slow oscillations in the MEC. Rhythmic Up States (US) could be recorded *in vivo*, and demonstrated stable frequency and duration over time. Using L3PC-specific expression of archaeorhodopsin in an Oxr1 x Ai40D crossed line, I found that pulsed LED stimulation decreased the frequency of US. These results were mirrored at a lesser magnitude using a closed-loop stimulation system. Further experiments with this paradigm, including with the L2 stellate cell (L2SC)-specific Uchl1-Cre line suggest that L3PCs control the incidence of US in the MEC in a layer- and cell-type specific manner.

In a second group of experiments, I studied the effects of L3PC silencing on spatial coding of pyramidal cells (PCs) in CA1, with a focus on theta phase precession (PP). To do so, I employed chronic silicon probe implants with a chemogenetic strategy (hM4D) targeting L3PC cells of freely-moving Oxr1-Cre mice. This led to the abolition of synaptic transmission in vitro, and modest increase of CA1 PC firing rate in vivo after systemic injection of hM4D clozapine-n-oxide (CNO). I determined that treatment with CNO *in vivo* did not have an effect on PP slopes, correlations, offsets or phase range as measured in a single-trial analysis. The presence of place cells, as well as their spatial properties, were also not altered by CNO treatment.

These findings demonstrate that L3PCs in the MEC are an important organizer of rhythmic activity during slow oscillations, but that they are not critical for PP and other spatial coding in CA1. This work may help draw a link between cell and layer-specific pathology in several conditions, as well as informing mechanistic explanations of cognitive symptoms.

2. Zusammenfassung

Seit den ersten Studien zu Amnesie am Patienten H.M. und den anschließenden Entdeckungen von funktionellen Zelltypen, die mit der Navigation verbunden sind, stehen der Hippocampus (HC) und der mediale entorhinale Kortex (MEC) im Mittelpunkt der Forschung zu Lernen und Gedächtnis. Die Aktivität dieser Gehirnstrukturen wird über neuronale Oszillationen koordiniert, die das Netzwerk in verschiedenen Frequenzen synchronisieren: unter anderem langsame- (Slow Oscillation < 1 Hz), Theta- (6 -11 Hz) Gamma- (40 – 100 Hz) und Ripple- (120 – 200 Hz) Oszillationen. Eine wichtige Rolle spielen hierbei Pyramidenzellen aus der dritten Zellschicht (L3PCs) des MEC, die in Area CA1 des Hippocampus projizieren. Dementsprechend lässt sich eine wichtige Rolle dieser Zellen für die Kommunikation zwischen dem HC und dem MEC vermuten.

Diese Arbeit untersucht die Rolle der L3PCs des MEC bei zwei Formen neuronaler Aktivität. Hierbei schaltete ich mit optogenetischen Werkzeugen L3PCs in einem anästhesierten Modell für Slow Oscillations im MEC aus. Synchronisierte, rhythmische Aktivitäten (‚Up States' (US)) wurden in vivo mit elektrophysiologischen Meßmethoden reliabel erfasst. Unter Verwendung von L3PC-spezifischer Expression von Archaeorhodopsin (Oxr1 x Ai40D), einem Konstrukt, welches lichtabhängig die zelluläre Aktivität inhibiert, konnte ich feststellen, dass gepulste LED-Stimulation die Häufigkeit von US verringert. Diese Ergebnisse spiegelten sich in geringerem Ausmaß bei Verwendung eines Stimulationssystems mit geschlossenem Regelkreis wider. Weitere Experimente, unter anderem mit der Schicht-2-Sternzellen (L2SC)-spezifischen Uchl1-Cre-Linie, legen nahe, dass L3PCs das Auftreten von US im MEC schicht- und zelltypspezifisch steuern.

In einer zweiten Gruppe von Experimenten untersuchte ich die Auswirkungen von L3PC-Inhibition auf die räumliche Kodierung von Pyramidenzellen (PCs) in CA1, mit einem Fokus auf die Theta-Phasenpräzession (PP). Dazu wurden chronische Silizium-Sondenimplantate mit einer chemogenetischen Strategie (hM4D), die auf L3PC-Zellen von freibewegenden Oxr1-Cre-Mäusen abzielte, verwendet. Dies führte zur Unterbrechung der synaptischen Übertragung *in vitro* und zu einem geringen Anstieg der CA1 PC-Feuerungsrate in vivo nach systemischer Injektion von hM4D-Clozapin-n-Oxid (CNO) *in vivo*. Ich stellte fest, dass die Behandlung *in vivo* mit CNO keinen Einfluss auf die Steigungen, die zirkulär-lineare Korrelation, Offset oder den Phasenbereich der in der Einzeltrial-Analyse gemessenen PP hatte. Das Vorhandensein von Place Cells sowie deren räumliche Eigenschaften wurden durch die CNO-Behandlung nicht verändert.

Diese Ergebnisse zeigen, dass L3PCs im MEC ein wichtiger Organisator von rhythmischer Aktivität und Slow Oscillations sind, aber dass sie nicht entscheidend für die PP und andere räumliche Kodierung in CA1 sind. Diese Arbeit kann dazu beitragen, eine Verbindung zwischen zell- und schichtspezifischer Pathologie bei verschiedenen Erkrankungen herzustellen, sowie mechanistische Erklärungen für kognitive Symptome zu liefern.

3. Introduction

The hippocampus (HC) and surrounding parahippocampal cortices have fascinated neuroscientists since first reports of anterograde amnesia after lesion of the temporal lobe in patient H.M. in the 1950s[1,2]. In the intervening decades, extensive studies, including the discovery of place cells and other cell types related to navigation[2], have meant that these structures remains a nexus of research on learning on memory in the brain. One of the most crucial elements in this network is the medial entorhinal cortex (MEC), which is the main cortical route of information flow in and out of the HC[3,4]. As the MEC is one of the earliest structures affected by Alzheimer's disease[5,6], and has a high susceptibility for epileptogenesis[7], there is a great interest in understanding its contributions to cortico-hippocampal communication.

In the healthy brain, rhythmic fluctuations, as measured by the local field potential (LFP), occur within HC-MEC network. These fluctuations are brought about by rhythmic de- and hyper-polarization of cells' membrane potentials, and thought to be crucial for synchronizing activity in the two structures[1]. LFP oscillations can occur at different frequencies which correlate with different behavioral states. For example, slow oscillations or so-called "up down states", propagate through the cortex at a frequency of < 1 Hz, accompanied by large irregular activity of the hippocampus during sleep[8,9]. In waking states, particularly during navigation, the HC and MEC also participate in theta oscillations, which are measurable as 8 – 11 Hz fluctuations of the LFP, often with nested gamma oscillations at 30 – 100 Hz[10–12].

Many researchers have proposed that alterations in network activity of MEC-HC connections may underlie cognitive deficits linked to learning and memory. For example, changes in slow oscillations correlated with HC-dependent memory consolidation have been described in humans with β-amyloid plaque pathlogy[13], as well as rodent models of epilepsy[14]. However, it is not clear precisely which connections between the MEC and HC are most important for different elements of synchronized network activity, nor which cells are most important for mediating them.

There are multiple pathways connecting the MEC and HC, which are both layer- and subregion-specific. These connections are dominated by two main projections: layer 2 stellate cells in the MEC (L2SCs) synapsing onto dentate granule cells in the dentate gyrus via the perforant path (i.e. the "indirect" path), and projections from layer 3 pyramidal cells (L3PCs) in the MEC entering CA1 via the temporoammonic pathway (i.e. the "direct" path)[3,15]. The former cell type, which

makes up the majority of principal cells in L2, has been extensively researched due to the discovery of grid cells in superficial layers of the MEC[16], and feeds spatial information forward to place cells in area CA1 via the dentate gyrus and area CA3[17].

MEC L3 is comprised of a large band of neurons with pyramidal morphology and varying dendritic arborization terminating mainly in L1[18–21]. The majority of these cells are notable for their long membrane time constant and high input resistance, leading to early speculation that they may be important for integrating and transmitting information from multiple sources[19,20]. Like L2SCs, L3PCs also code for spatial aspects of the environment[22,23], yet with generally lower theta rhythmicity, spatial modulation, and regular spatial firing than L2SCs[24–27]. L3PCs also send a robust feedforward projection to L2SCs, which have extremely low connectivity among themselves[28,29]. Thus, L3PCs have the potential to be an important driver of MEC-HC communication, as they can potentially transmit information through both the direct and indirect pathways.

Studies of cortico-hippocampal communication between MEC and CA1 have shown than inactivation of superficial layers of the MEC leads to profound changes in behavior and learning. These changes are evident on the level of population coding and oscillations[30–33], as well as hippocampal coding of space via place cells (see for example[30–36]). However, most of these studies have not been able to differentiate cell type-specific effects of silencing L2SCs and L3PCs (for notable exceptions, see below).

3.1 The role of the MEC in up down states

Slow oscillations have been observed throughout the brain in both rodents and humans during natural sleep, quiet awake states, and under anaesthesia[8,9]. On a cellular level, these oscillations are linked to a bimodal rhythmic alternation between a depolarized and hyperpolarized membrane potential, otherwise known as “up down states” (UDS). UDS propagate through the cortex in a stereotyped manner[37,38], and many studies have shown that distinct populations of excitatory and inhibitory cortical cells are responsible for controlling their initiation, spread, and termination[8,9,39,40]. More recently, it was shown that UDS aid in synapse elimination and refinement of memory traces during sleep[41,42].

Through both *in vitro* preparations with young tissue[39,40,43] and *in vivo* preparations in adult anaesthetized and sleeping mice[44,45], it was discovered that L3 is the most active cell layer in the MEC during up states (US). Critically, it was found that L3PCs display persistent activity during US *in vivo*, and can bias multiunit activity in area CA1 of the HC[44,45]. Thus, it is likely that they initiate US in the MEC, and excite other cell layers and regions via their feed-forward projections.

Despite all that is known about the MEC and its activity during UDS, several questions remain. First, L3PCs' orchestration of UDS in the MEC has never been causally tested or controlled *in vivo.* Additionally, it is not known whether silencing other cell layers, such as L2SCs, also has the potential to disrupt the local LFP during UDS. A better understanding of the propagation of UDS through different layers of the MEC could have important implications for understanding how the MEC gates information flowing in and out of the HC during slow oscillations.

3.2 The role of the MEC in phase precession

Due to their prominent projection to area CA1 of the HC, MEC L3PCs also been studied for their contribution to the activity of HC place cells during navigation. Recent studies using the L3PC-specific mouse line oxidation resistance 1 (Oxr1) - Cre have found that silencing of these cells leads to reduced gamma synchrony between MEC and CA1[32], tied to impairment in a spatial memory task (see also[46]). Yamamoto and Tonegawa[33] also found more fragmented place cell sequences in sharp-wave ripple-mediated replay in awake animals. Interestingly, none of these studies found major changes in the properties of CA1 place cells themselves after L3PC silencing. These findings suggest L3PCs may be more important for the temporal structure of MEC-HC activity than "pure" spatial coding. On the other hand, Bittner and colleagues[47] found that optogenetic silencing of L3PCs led to reduced ramp amplitude and initiation of dendritic plateau potentials (associated with new place field formation) in CA1 pyramidal cells in a virtual reality navigation task. These findings suggest that place cell activity is driven by conjunctive input from both CA3 and L3PCs input on a fine timescale.

Thus it seems that MEC L3PCs could play an important role in both the temporal structure of population activity during UDS and temporal aspects of spatial coding. One explanation for this influence could be the role of MEC L3PCs in theta phase precession (PP) in the HC. PP, first identified by O'Keefe and Recce[48], is the phenomenon whereby the theta phase (i.e. its position of a spike from 0 - 360° in an idealized version of a single theta cycle) of place cell spikes is

negatively correlated with an animal's position in a place field. As an animal moves through a place field, spikes occur earlier relative to the phase of the ongoing theta oscillation, meaning that in addition to the rate of firing, the animal's position is also coded by phase. Phase coding has been hypothesized to augment the information content of place cells, as it has been shown to allow more accurate decoding of location and trajectory than rate alone[49–51]. In turn, spikes clustered in a temporally meaningful way could aid in compression of behavioral sequences[52] and allowing for NMDAR-dependent spike-timing dependent plasticity[52,53].

Three lines of evidence provide support for an important role of L3PCs in hippocampal PP. First, the activity of CA1 place cells during exploration is biased by input from MEC L3PCs and CA1 cells fire close to the preferred phase of L3PCs input[54]. In addition, CA1 cells showing the highest quality of PP likely receive more projections from L3PCs than area CA3[51,54,55]. Second, theoretical and modelling work shows that PP in CA1 could be inherited from another structure[56,57]. Due to their feedforward projections to L2SCs in MEC microcircuitry[28,58] unique long membrane time constants and slow decay of excitatory post-synaptic potentials [19–21], and own spatial coding and PP [22–24,59], L3PCs are a strong candidate for providing feedforward spatial information or temporal structure to place cells in CA1.

The final line of evidence comes from work examining the effect of MEC lesions on PP in area CA1. Using different methods, Schlesiger et al.[36] and Ormond et al.[30] discovered that lesioning or pharmacologically silencing superficial layers in the MEC led to weakening of CA1 PP, as well as a general decrease in the specificity and quality of place coding. However, due to non-cell type specific interventions, it is impossible to determine whether these effects were due to effects on L2SCs, L3PCs, or even other structures. These studies, as well as other theoretical works[56,57], hypothesize that inputs from MEC L2SCs to the dentate gyrus and area CA3 (i.e. the 'indirect pathway') could also have important effects on spatial coding in CA1. While a recent study interestingly showed no evidence of an effect of silencing CA3 pyramidal cells on CA1 PP[60], the exact contributions of L3PCs and L2SCs to CA1 spatial coding remain complex and poorly understood[3].

3.3 Goal and hypotheses

The central he goal of the work in this thesis is to better understand the role of MEC L3PCs in mediating MEC-HC communication using electrophysiological *in vivo* techniques in mice. This

was undertaken in two ways. First, I studied the role of L3PCs in the initiation of US within the MEC. I hypothesized that L3PCs cells are powerful mediators of US, and silencing them could reduce detectable deflections in the LFP. Second, I tested whether L3PCs are a critical driver of PP and spatial properties of place cells in area CA1 of the HC during navigation. Here, I hypothesized that silencing L3PCs would lead to a decrease in the quality of PP, measured via slope and circular-linear correlation, but leave other spatial coding properties of place cells intact.

4. Methods

4.1 Mice and husbandry

Experiments were performed in adult mice (p30+, 20 - 35 g) of both sexes in the following strains: C57Bl6/n (wildtype, WT), Oxr1-Cre (JAX stock #030484, see also[46]), Oxr1-Cre x Ai40D (Archaerhodopsin-3/EGFP fusion protein, ArchT-EGFP) crosses (JAX stock #030484; JAX stock #021188), and Uchl1 (Ubiquitin C-Terminal Hydrolase L1)-Cre (MMRC, USA; see also[61]). Mice were housed with a 12-hour light/dark cycle in group cages, with *ad libitum* access to water and standard rodent chow. All experiments were performed in accordance with guidelines of the Berlin Office of Health and Social Affairs (G0092/15, G0150/17, and G0189/17).

4.2 Viral injections

Mice were deeply anaesthetized with 2% isofluorane and a craniotomy performed, exposing the transverse sinus. Viral injections were performed at an angle -8° in the antero-posterior axis at the following coordinates: 0.2 mm (target: MEC L2) or 0.3 mm (target: MEC L3) anterior to transverse sinus, ±3.3 ML, 1.8 DV. Halorhodopsin (NpHR) was expressed using the viral construct pAAVEf1a- DIO eNpHR 3.0-EYFP (a gift from Karl Deisseroth; Addgene viral prep # 26966-AAV1). Virally-expressed hM4D Designer Receptors Exclusively Activated by Designer Drugs (DREADDs), which shut down axonal synaptic transmission by activating intracellular $G_{i/o}$ intracellular signalling pathways[62], were expressed using the viral construct pAAV-hSyn-DIO-hM4D(Gi)-mCherry. Channelrhodopsin (ChR2) for *in vitro* experiments was expressed using pAAV-EF1a-double floxed-hChR2(H134R)-EYFP), and was mixed at a ratio of 25:75 with the hM4D construct. All injections used 500nL of viral construct injected bilaterally, except for the ChR2 - hM4D mix, which was injected into the right hemisphere only. After surgery, mice were provided with carprofen and metamizol and were monitored for weight and general health daily thereafter.

4.3 *In vitro* CNO recordings

In vitro recordings for testing efficacy of CNO in Oxr1-Cre mice were performed by colleagues P. Beed, D. Parthier and A. Stumpf, using optogenetic connectivity mapping, as described in more detail elsewhere (see[63]). Briefly, acute horizontal 400ųm slices were prepared from the MEC of Oxr1-Cre injected with hM4D and ChR2 constructs. Cells downstream from L3 of the MEC (e.g. in layer 5b of the MEC[64,65]) were measured in whole-cell patch-clamp configuration. ChR2-expressing fibers in the area were activated using 3x10 ms light pulses at 10 Hz from a LED (CoolLED pE-2, Andover, UK). If existing connections were established, 10 µM CNO (hellobio, Bristol, UK) were washed in while stimulation was performed in regular intervals (15 s) using the previous light stimulation protocol.

4.4 Anaesthetized recordings

Mice for UDS recordings (n = 9 WT, 7 Oxr1 x Ai40D, 3 Uchl1-Cre) were deeply anaesthetized by intraperitoneal injection of a 10% urethane solution (1-1.5g/kg, Sigma Aldrich). 32-channel linear silicon probes or optrodes (NeuroNexus) were painted with the fluorescent dye DiI (Thermo Fisher Scientific) and lowered slowly into the craniotomy at a 20° angle in the sagittal plane. An Ag/AgCl ground wire was placed into a well with saline above the frontal cortices. Signals were sampled at 20 kHz with an RHD2000 amplifier (Intan Technologies), and visualized using on-board recording software. Recordings began after a 10 minute waiting period at a depth at which clear up states could be seen at a frequency of approximately 0.1 Hz. For optogenetic pulse barrage experiments, a 10 minute baseline (light OFF) was first recorded. Next, a 10 Hz light ON protocol (for 5 seconds) was applied using a 525 nm PlexBright LED (Plexon) coupled directly to the silicon optrode. This was repeated after a 5 second light OFF period. These dual barrages were repeated every 10 seconds over 20 minutes. In a second set of experiments, a closed-loop optogenetic stimulation system was created by routing one channel of the LFP via a National Instruments BNC-2110 shielded connector block to a computer running Simulink (Mathworks). Whenever a threshold-crossing event was detected, a pulse was emitted to the LED, with a delay of approximately 50 ms (data not shown).

4.5 Behavioral setup

After injection, DREADD-injected Oxr1-Cre mice (n = 4) were handled daily and habituated to the chronic recording environment. This consisted of a 10 x 80cm hallway with walls of 10 cm.

All training and subsequent recordings were performed under illuminated conditions, with visual cues available on all 4 sides.

4.6 Chronic silicon probe implants

After 5 weeks' recovery and incubation time, hM4D-injected Oxr1-Cre mice for place cell recordings were anaesthetized with 2% isofluorane, and a ground screw was affixed over the left cerebellum. A crainiotomy and durectomy were performed at the coordinates 1.8 AP and +1.8 ML. A 32-channel silicon probe mounted on a d-Drive (NeuroNexus), and painted with fluorescent DiI (Thermo Fisher Scientific), was lowered to a depth of 0.9 mm from the skull surface, and attached to the skull using OptiBond (Kerr), Charisma composite, and dental cement (both Kulzer). The crainiotomy was sealed with a mixture of paraffin oil and bone wax. Reference and ground wires from the silicon probe were soldered to the cerebellar screw and a small Faraday cage was soldered around the implant for shielding. Mice were provided with carprofen and metamizol and left for at least 3 days to recover.

4.7 Chronic recordings

After the implantation surgery and recovery in DREADD-injected Oxr1-Cre mice, the silicon probe was lowered approximately 0.3 ɥm daily until stable hippocampal units were detected using the same Intan recording system as described above. Thereafter, every day a 20 minute baseline session was recorded. Mice were then injected intraperitoneally with the DREADD agonist CNO dihydrochloride (1mg/kg) (hellobio) and placed back in their home cages to rest for one hour before beginning a 20 minute test recording. The following day, the baseline and test sessions were repeated with sterile saline (NaCl). This sequence was repeated for approximately 2 weeks. The position of the mouse during recordings was detected via an LED soldered to the headstage, and synchronized with the electrophysiological signal using a custom data acquisition pipeline created with the software Bonsai[66].

4.8 Analysis of anaesthetized recordings

All analysis was performed offline using custom scripts written in Matlab (Mathworks; https://github.com/Schmitz-lab/MEC-Up-States). First, a channel was selected from the tip of the silicon probe in L3 or L2, and down-sampled from 20 kHz to 200 Hz. US were detected using a modified version of the Moving Averages for Up and Down Separation (MAUDs) algorithm[67]. Briefly, the LFP was filtered between 1 and 4 Hz, and smoothed using a Savitzky-Golay filter.

Using a moving window, deflections 2 standard deviations above the median were calculated and compared with periods of elevated multiunit activity extracted with Kilosort2[68] to find indices of US. From these indices, the spectral content of these US could be calculated with the Stockwell Transform[69]. The effect of LED pulse barrages was calculated by detecting the number of US occurring inside of stimulation epochs, and comparing it to light OFF epochs of equivalent length (i.e. 50 ms) randomly sampled from the rest of the recording. The effect of closed loop stimulation was calculated by comparing the properties of US detected in 10-minute baseline (light OFF) and stimulation (light ON) sessions.

4.9 Analysis of chronic recordings

All analysis of recordings of chronically implanted mice was performed using custom scripts written in Matlab (Mathworks; repository in preparation and code freely available on request), including code from the buzcode repository (https://github.com/buzsakilab/buzcode/wiki). Recordings were spike sorted using Kilosort2[68], and manually curated. The quality of putative units was assessed by calculating (i) the Isolation Distance, (ii) L-ratio, and (iii) refractory period violations[70]. Using a k-means algorithm with the parameters spike asymmetry, mean firing rate and full-width at half maximum[71], units were sorted into groups corresponding to putative pyramidal cells (PCs) and interneurons (INs). In order to lower the risk that slow-firing interneurons might erroneously have been included in this characterization, putative PCs were further restricted to units with a mean firing rate < 5 Hz.

Epochs of PP were identified using a temporal clustering method adapted from Aghajan et al.[72], see also[73]. Briefly, spike trains were convoluted with a Gaussian kernel of width 100 ms, and screened for periods in which the firing rate was above 5 Hz. These candidate runs were expanded forward and backwards in time with a window until the firing rate dropped < 10% for more than 250 ms (ca. 2 theta cycles). Each individual run was required to have a duration of 300 ms and a minimum average speed > 5 cm/s. The phase of the spikes from these runs was extracted from the Hilbert transform of the filtered (6 -11 Hz) LFP. PP was measured on a single-run basis using circular-linear correlation, permitting extraction of (i) the slope of a regression line (deg/s) (ii) a circular-linear correlation coefficient (r), (iii) the phase offset of the line of regression (deg) and (iv) a measure of phase range in a given precession epoch (slope x time, deg)[50,74,75,76]. Slopes greater than three times the population interquartile ratio were excluded, as were their corresponding correlations, offsets, and phase ranges.

For calculating spatial information related to each neuron, a speed threshold of 3 cm/s was applied to distinguish periods of rest and movement. To generate firing rate maps, the arena was divided into 1.25cm x 1.25cm bins. For each bin, the occupancy of each bin over time was calculated using a Gaussian smoothing kernel of $\sigma = 1$ s. Spatial information (I, bits/spike) was calculated using a cell's firing rate as a function of location over time[77].

For definition of place cells, firing rate maps were first created as defined above. Putative fields were first defined by identifying contiguous bins with an area of at least 10 cm^2 and an average firing rate of at least 50% of a cell's peak firing rate. Spatial coherence was calculated by correlating the z transform of the correlation between a pixel and the firing rate of its 8 neighbors after smoothing[78]. Fields with a coherence measure > 0.5 were defined as putative place fields. Sparsity, a measure of place field coverage of the environment, was defined using a method adapted from Skaggs[52].

4.10 Histology

After all recordings were completed, mice were deeply anaesthetized and given an overdose of urethane, then perfused transcardially with 0.1M phosphate-buffered saline (PBS) followed by 4% paraformaldehyde. Brains were kept in PFA overnight, then sliced using a vibratome (Leica Microsystems) into 100 μM (MEC) or 50 μM (HC) sagittal slices and mounted for post hoc anatomical identification of recording sites and immunohistochemical stainings.

Slices were incubated in PBS containing 1% Triton X-100 and 5% normal goat serum for 4 hr at room temperature (RT). Slices were incubated with primary antibodies for 48 hr at RT. After rinsing two times in 0.1M PBS, sections were incubated in the PBS solution containing 0.5% Triton X-100 and secondary antibodies. The following primary and second antibodies combinations were used: WFS1 (1:1000, Rabbit, Proteintech) and anti-rabbit Alexa fluor 647 (1:500, Invitrogen) for visualizing the borders of CA1; AntiGFP (1:1000, Chicken, Abcam) for amplifying signal of cells expressing Arch in Oxr1-Cre x Ai40D mice; Anti-NeuN (1:1000, Guinea Pig, Merck) and anti-guinea pig Alexa fluor 488 (1:500, Invitrogen) for visualizing neuronal cell bodies. Slices were mounted in Mowiol (Sigma Aldrich) under coverslips 2-3 hours after incubation with the secondary antibodies and stored at 4 °C.

4.11 Quantification and statistical analysis

No randomization and blinding were performed for experiments in this thesis, nor were sample sizes determined *a priori*. For prespecified analysis plans of PP data, please see study preregistration (https://osf.io/crqpu). Statistical tests were performed with Matlab (Mathworks) and Graphpad Prism. Normality was assessed using the Kolmogorov-Smirnov test, and data failing this assumption were analyzed using non-parametric tests. All tests were two-tailed. Data are presented as median ± inter-quartile range (IQR) unless otherwise noted. Significance was determined at $p < 0.05$ and labeled as: n.s. (not significant) for $p > 0.05$, * $p < 0.05$ and ** $p < 0.01$.

5. Results

5.1 Inhibition of L3PCs during up down states in the MEC

The first group of experiments in this thesis examine whether L3PCs are critical for initiation of UDS in the MEC. Here, I began by establishing an *in vivo* model. First, using silicon probes positioned in wildtype mice anaesthetized with urethane, I recorded slow UDS oscillations, containing nested gamma oscillations, in MEC L3 (**Figures 1a-c**). These oscillations were stable over time, and demonstrated consistent frequency and duration (**Figure 1d**: mean frequency ± standard error of mean (SEM) in the first 5 min = 0.15 ± 0.012 Hz; last 5 min = 0.15 ± 0.056 Hz; $p = 0.82$, $U = 11$; mean duration ± SEM in first 5 min = 1.86 ± 0.32 s, last 5 min = 1.53 ± 0.95 s; $p = 0.42$, $U = 8$, Mann-Whitney U test, $n = 5$ recordings from 5 mice).

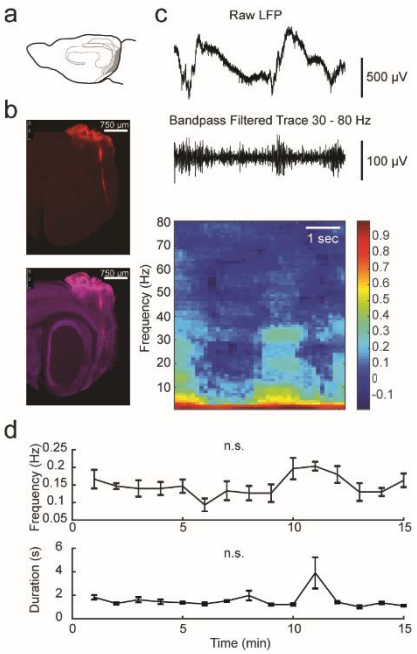

Figure 1. Up states in the MEC recorded in vivo

(A) Schematic drawing of the MEC (grey) in a sagittal view. **(B)** Example histology from an MEC recording, showing a sagittal section with track of silicon probe in L3 (top, red) and overlay with NeuN neuronal cell body staining (bottom, violet). **(C)** Raw LFP trace from recording (top) with highlighted nested gamma frequency oscillations (middle, band-pass filter from 30 to 80 Hz applied). Lower panel shows spectrogram of above trace created using a Stockwell transform. **(D)** Plot of stable detected up state frequency and duration over 15 minutes of recording (n = 5 recordings from 5 mice). Data presented as means ± standard error of the mean, n.s. for p >. 0.05. *Adapted from Figure 1 of Beed, De Filippo, Holman et al. 2019*[79].

If L3PCs are the driving force behind UDS in the MEC, then silencing these cells should lead to a large reduction in detectable UDS in the LFP. We therefore crossed the Oxr1-Cre and Ai40D mouse lines, allowing for the selective expression archaeorhodopsin (Arch) in L3 of the MEC. In subsequent experiments, I used an optrode to silence Arch+ L3PCs directly at the recording site using a pulsed light protocol (**Figure 2a,** see also **Methods**). Silencing L3PCs in this way lead to a large reduction in the frequency of detected US (**Figure 2b:** light OFF of 1.58 ± 0.68 Hz, light ON = 0.34 ± 0.18 Hz). This corresponded to or an average reduction of 79.1% ($p = 0.016$, $Z = -2.37$, Wilcoxon signed rank test, n = 7 recordings from 7 mice).

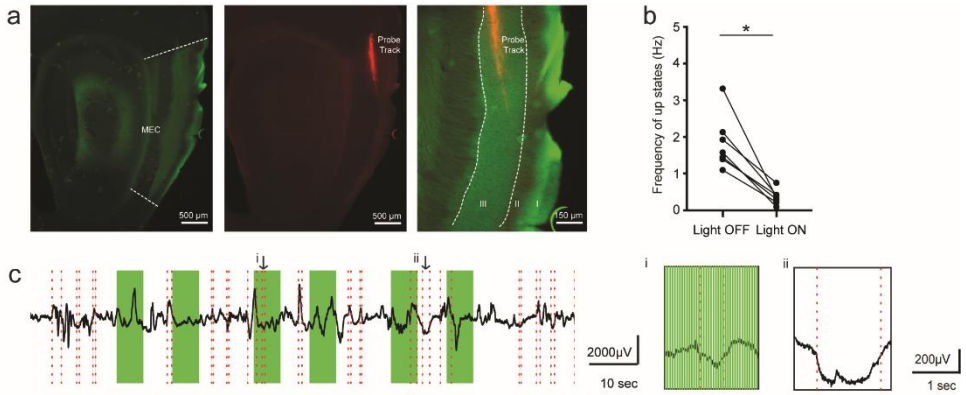

Figure 2. Up state recording with LED activation in vivo
(A) Example histology from an MEC recording in Oxr1 x Ai40D mice, showing a sagittal section with constitutive Arch and GFP expression (left, green), a track of a silicon probe (middle, red), and 10x merge (right). **(B)** Frequency of detected up states in light OFF compared to light ON periods (n = 7 recordings from 7 mice). **(C)** Example trace from an optrode recording in L3 of the MEC. Green bars indicate LED activation (light ON) and red dotted lines represent beginning and end of detected up states. Two example up states indicated by i and ii are shown magnified (right). * = significance at $p < 0.05$. *Adapted from Figure 3 of Beed, De Filippo, Holman et al. 2019*[79].

I next sought to control MEC US in a more time-locked manner, using a closed-loop system that permitted LED activation with a delay of approximately 50 ms every time the beginning of a large LFP deflection was detected in Oxr1 x Ai40D mice (**Figure 3a-c**). Here, LED stimulation also resulted in lowered frequency of detected US, but in a non-statistically significant manner (**Figure 3d**: light OFF = 0.27 ± 0.25 Hz, light ON = 0.14 ± 0.19 Hz; $p = 0.13$, $Z = -1.75$, Wilcoxon signed rank test). The duration of US in these mice was unchanged (**Figure 3e**: light OFF duration = 1.13 ± 1.57 s, light ON duration = 1.32 ± 1.56 s; $p = 0.063$, $Z = -2.023$, Wilcoxon signed rank test, n = 5 recordings from 5 mice). I next sought to test this system in other mouse lines.

L2SCs are downstream from L3PCs[28,29]. As related *in vitro* experiments pointed to the possibility that UDS propagate to deep layers of the MEC (see Beed, de Filippo, Holman et al. 2020[79]), I wanted to determine whether silencing L2SCs during US could also have an effect on the local LFP, confounding interpretation of disruption of L3PCs on deep layer activity (see e.g. Figures 4 and 5 in Beed, De Filippo, Holman et al., 2020). Thus, I used the Uchl1-Cre line, which expresses Cre in L2SCs[61]. I injected these mice with a viral construct bearing the inhibitory opsin halorhodopsin (NpHR) (**Figure 4a**) and subjected them to the same closed-loop stimulation protocol as above (**Figure 4b**). Here, there was no effect on the frequency or duration of detectable up states (**Figure 4c**: frequency: light OFF = 0.25 ± 0.22 Hz, light ON = 0.31 ± 0.17 Hz; $p = 0.13$, $Z = -1.83$; **Figure 4d**: duration: light OFF = 1.61 ± 0.92 s, light ON = 1.52 ± 0.67 s; $p = 0.14$, $Z = 1.46$, Wilcoxon signed rank test, n = 4 recordings from 3 mice).

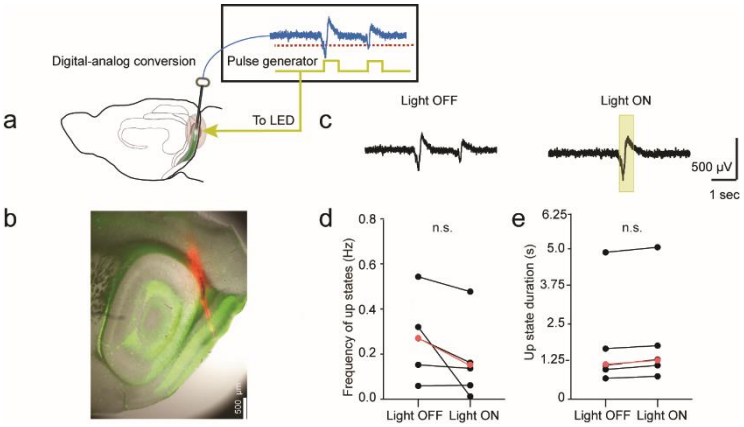

Figure 3. Up state recording using a closed-loop system

(A) Schematic showing LED pulse emission after detected deflection of the LFP during recording using a closed-loop system. **(B)** Example histology from optrode closed-loop recording in L3 in Oxr1 x Ai40D mice, showing bright field image (grey), cell fibers expressing Arch and GFP (green), and probe track (red). **(C)** Example local field potential from baseline (left, light OFF) and light ON periods (right), with yellow rectangles indicating periods of stimulation. **(D)** Average frequency (Hz) of detected up states in Oxr1 x Ai40D mice during light OFF and light ON periods. (n = 5 recordings from 5 mice) **(E)** Average duration (s) of detected up states in Oxr1 x Ai40D mice during light OFF and light ON periods (n = 5 recordings from 5 mice). For all line graphs in this figure: Points connected by black lines indicate individual recordings and red points lines indicate median. N.s. at $p > 0.05$. *Adapted from Figure S4 of Beed, De Filippo, Holman et al. 2019*[79].

Finally, I also performed the same closed-loop inhibition protocol on non-injected WT mice to exclude non-specific effects of LED illumination of the MEC under anaesthesia (**Figure 4e-h**). There was also no significant effect of LED illumination on the frequency or duration of US (**Figure 4g**: frequency: light OFF = 0.14 ± 0.067 Hz, light ON = 0.22 ± 0.18 Hz; p = 0.19, Z = -1.48; **Figure 4h**: duration: light OFF = 1.46 ± 0.51 s, light ON = 1.49 ± 0.534 s; p =0.31, Z = -1.21, Wilcoxon signed rank test, n = 5 recordings from 5 mice).

Comparing all three groups (Oxr1 x Ai40D, Uchl1-Cre x AAV-eNpHR3.0-EGFP and WT), I found that Oxr1 x Ai40D mice had a decreased (but non-significant, p = 0.050) normalized (light OFF/light ON) frequency of US compared to the other lines using the closed-loop protocol (**Figure 4i**: p = 0.050, H = 5.6, Kruskal Wallis Test, n = 5, 4, and 5 recordings). A Dunn's multiple comparisons test revealed that closed-loop stimulation produced a slight difference in frequency for Oxr1 x Ai40D compared to wild-type mice (p = 0.047). No significant difference was found between WT and Uchl1-Cre x AAV-eNpHR3.0-EGFP mice (p > 0.99). Thus, taken together with pulsed light experiments, it seems that L3PCs cells are a likely play a key role in initiation of US *in vivo*, and that inhibiting their activity leads to a reduction of detectable US in the MEC. Elaboration on these findings *in vitro* may be found in Beed, De Filippo, Holman et al., 2020[79].

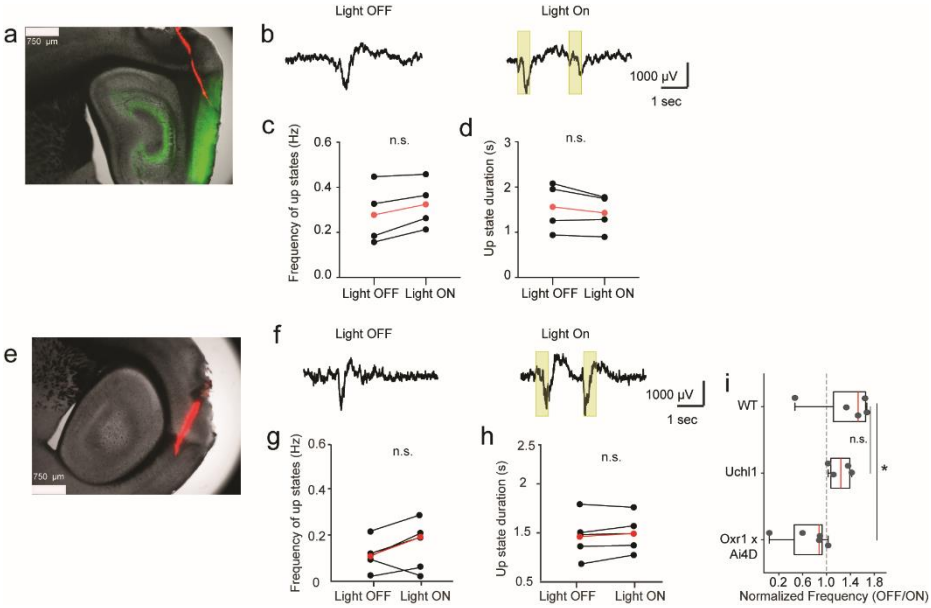

Figure 4. Up state recording in Uchl1-Cre and WT mice

(A) Example histology from optrode closed-loop recording in L2 in Uchl1-Cre x AAV-eNpHR3.0-EGFP mice, showing bright field image (grey), cell fibers expressing NpHR and EGFP (green), the probe track (red). **(B)** Example local field potential from baseline (left, light OFF) and light ON periods (right), with yellow rectangles indicating periods of stimulation. **(C)** Average frequency (Hz) of detected up states in Uchl1-Cre mice during light OFF and light ON periods. For all line graphs in this figure: Points connected by black lines indicate individual recordings and red points and lines indicate median (n = 4 recordings from 3 mice). **(D)** Average duration (s) of detected up states in Uchl1-Cre mice during light OFF and light ON periods (n = 4 recordings from 3 mice). **(E)** Example histology from optrode closed-loop recording in L3 in wildtype mice, showing bright field image (grey) and probe track (red). **(F)** Example raw traces from baseline (left, light OFF) and light ON periods (right), with yellow rectangles indicating periods of stimulation. **(G)** Average frequency (Hz) of detected up states in wildtype mice during light OFF and light ON periods (n = 5 recordings from 5 mice). **(H)** Average duration (s) of detected up states in Uchl1-Cre mice during light OFF and light ON periods (n = 5 recordings from 5 mice). **(I)** Comparison of detected up state frequency (Hz) in light ON periods normalized to light OFF periods, in recordings from wildtype mice (top), additionally showing recordings from Uchl1-Cre mice (middle) and Oxr1 x Ai40D (bottom). Red lines indicate medians of each group, with box edges extending to 25th and 75th percentile. Whiskers extend to most extreme data points (n = 5,4, and 5 recordings from 4, 3, and 5 mice). * = significance at $p < 0.05$, n.s. = not significant at $p > 0.05$. *Adapted from Figure S4 of Beed, De Filippo, Holman et al. 2019*[79].

5.2 Inhibition of L3PCs and exploration of spatial coding in area CA1

While L3PCs appear to play a role in UDS in the MEC, it is not clear if they also are important in other behavioral contexts. In the second portion of this thesis, I sought to clarify the role of L3PCs in temporal organization of spatial activity in CA1 in mice exploring a linear track. To do so, I used a chemogenetic strategy with hM4D-injected Oxr1-Cre mice, allowing selective expression of DREADDs in L3PCs of the MEC and silencing their projections to CA1 by systemic injection of CNO. Before beginning *in vivo* measurements, the efficacy of CNO was tested with colleagues *in vitro* by injecting Oxr1-Cre mice with both viruses bearing ChR2 and hM4D, and preparing acute slices for patch clamp measurements. Connectivity to patched cells downstream of layer 3 (e.g. in layer 5b[64,65]) could be established by stimulating axonal fibers expressing ChR2, and abolished by washing in CNO (data not shown).

In vivo experiments began with injection of hM4D into Oxr1-Cre mice (n = 4), followed by several weeks of habituation in the recording arena and surgical implantation of a chronic silicon probe (**Figure 5a-b**). Every recording day began with a 20 minute baseline, followed with intraperitoneal injection of either CNO or NaCl (a control for stress caused by injection or handling). Mice were placed back in their home cages for an hour to allow the CNO to take effect[62], followed by a 20 minute "test" session back on the linear track. In total, 22 baseline, 12 CNO and 10 NaCl sessions were successfully performed on the linear track. Spike sorting yielded a total of 257 units, which were sorted into putative PCs and INs using k-means clustering (**Figure 5c**). Further quality controls on the basis of Isolation Distance, L-ratio and violations of inter-spike interval refractory periods yielded 37 putative pyramidal cells and 73 putative interneurons for further analysis (e.g. **Figure 5d**).

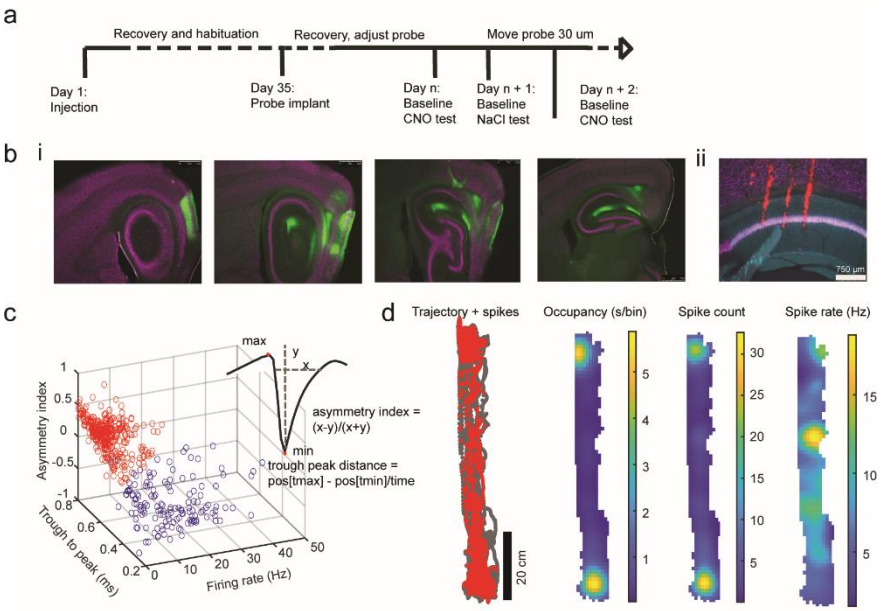

Figure 5. Design of in vivo experiments and cellular analysis
(A) Simplified timeline of in vivo experiments. **(B)** (i) Example sagittal sections from Oxr1-Cre mouse injected in L3 with hM4D, showing infected cell fibers (green) merged with NeuN (violet). (ii) Detail of CA1, showing cell bodies stained with NeuN (violet), CA1 pyramidal cells stained with Wfs1 (blue), and probe tracks (red). Note: the 4th probe track appears in a subsequent section. **(C)** K-means clustering of all clusters in a dataset, contrasting the trough to peak distance (x axis), asymmetry index (y axis) and firing rate (z axis). Red and blue points show clustered that were classified as putative PCs and INs, respectively. Inset shows calculation of parameters from average waveforms of individual clusters fed into the classifier **(D)** Example processing of locating and spiking from a putative pyramidal cell, showing (left – right) spikes (red) superimposed on the mouse's trajectory (grey), occupancy calculated as time (s) spent in each 1.25 x 1.25 cm bin, spike count in each bin, and resulting rate map calculated based on occupancy and spike count. *Original figure.*

To ascertain broad effects of L3PC on activity in CA1, I compared the firing rate of PCs between baseline and CNO session, with NaCl sessions as a control (**Figure 6a**). It was found that the firing rate of CA1 PCs with CNO slightly increased compared to the baseline (**Figure 6a**: baseline =

1.43 ± 1.79 Hz; CNO =1.80 ± 1.24 Hz, p = 0.035, n = 24 cells, Wilcoxon signed rank test. Note slight shift of cell population to the left). There was no effect on firing rate in NaCl sessions, indicating the effect was treatment-specific (**Figure 6a:** baseline = 1.81 ± 1.94 Hz, NaCl = 3.02 ± 1.86 Hz, p = 0.38, n = 13 cells, Wilcoxon signed ranks test). The baseline firing rates of PCs for sessions that subsequently received CNO or NaCl did not differ (Data not shown: pre-CNO baseline = 1.43 ± 1.79 Hz, pre-NaCl baseline = 1.801 ± 1.94 Hz; p = 0.36, U = 116, Mann-Whitney U test, n = 24 and 13 cells from 4 mice).

Interestingly, the firing rate of CA1 INs did not significantly change in the presence of CNO (**Figure 6b**: baseline = 12.78 ± 8.8818, CNO = 10.17 ± 9.09; p = 0.45, n = 43 cells), or NaCl (baseline = 12.63 ± 8.98, NaCl = 13.69 ± 7.23; p = 0.27, Wilcoxon signed rank test, n = 33 cells from 4 mice). Thus, it seems that CNO silencing of projections from L3PCs selectively had mild effects on the firing rate of CA1 PCs.

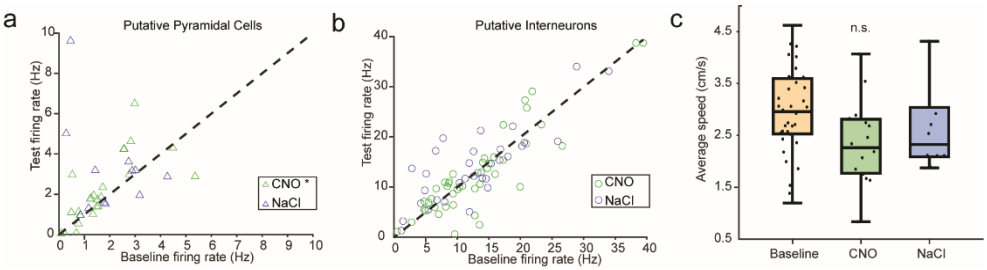

Figure 6: Effects of treatment with CNO and NaCl in vivo

(A) Average firing rates of putative pyramidal cells (triangles) across baseline (x axis) and test (y axis) sessions. Green points indicate test sessions with CNO, blue points represent test sessions with NaCl. Dotted black line represents identity. Note shift in CNO data points to left of line. N = 37 cells from 4 mice. **(B)** Average firing rates of putative interneurons (circles) across baseline (x axis) and test (y axis) sessions. Green points indicate test sessions with CNO, blue points represent test sessions with NaCl. Dotted black line indicates identity. N = 43 cells from 4 mice. **(C)** Comparison of average speed (cm/s) during baseline (yellow, left), CNO (green, middle) and NaCl recordings (blue, right). Horizontal black lines indicate group medians, with box edges delineating 25th and 75th percentiles. Box whiskers extend to most extreme data points. N = 22, 12 and 10 recordings from 4 mice. * = significance at $p < 0.05$, n.s. = not significant at $p > 0.05$. *Original figure.*

CNO has been reported to have effects on locomotion in rodents[80], and firing rates in CA1 increase with running speed[81]. Thus, I compared average speed in baseline CNO and NaCl sessions. There was no difference in the average speed between session groups (**Figure 6c**; baseline = 2.99 ± 1.06, CNO = 2.33 ± 1.03, NaCl = 2.33 ± 0.81; p = 0.062, H(2) = 5.58, Kruskal-Wallis test, n = 22, 12 and 10 sessions from 4 mice). Taken together, these findings show some efficacy of CNO-induced inhibition of L3PC, resulting in a slight increase in the firing rate of PCs without effects on locomotion.

To study L3PCs' effect on spatial coding in area CA1, PP epochs were identified on a single-run basis (**Figure 7a-d** and **Methods**), and circular-linear correlation was performed to determine the slope, correlation, offset and phase range in each epoch. (**Figure 7d**). Runs were pooled between all mice (see e.g. **Figure 7f - i**), and above parameters compared across recording sessions. The slopes of individual runs showed high variability, and there was not significantly different between baseline, CNO and NaCl sessions (**Figure 7f**: baseline = -11.63 ± 337.28 deg/s, CNO = -5.59 ± 269.49 deg/s, NaCl = 1.11 ± 288.23 deg/s; p = 0.39, H(2) = 1.88, Kruskal-Wallis test). Note that although the PP algorithm identified many incidences of phase *re*-cession (i.e. positive PP slopes), the medians of baseline and CNO sessions were still negative, in agreement with a previous single-trial reports in area CA1[76].

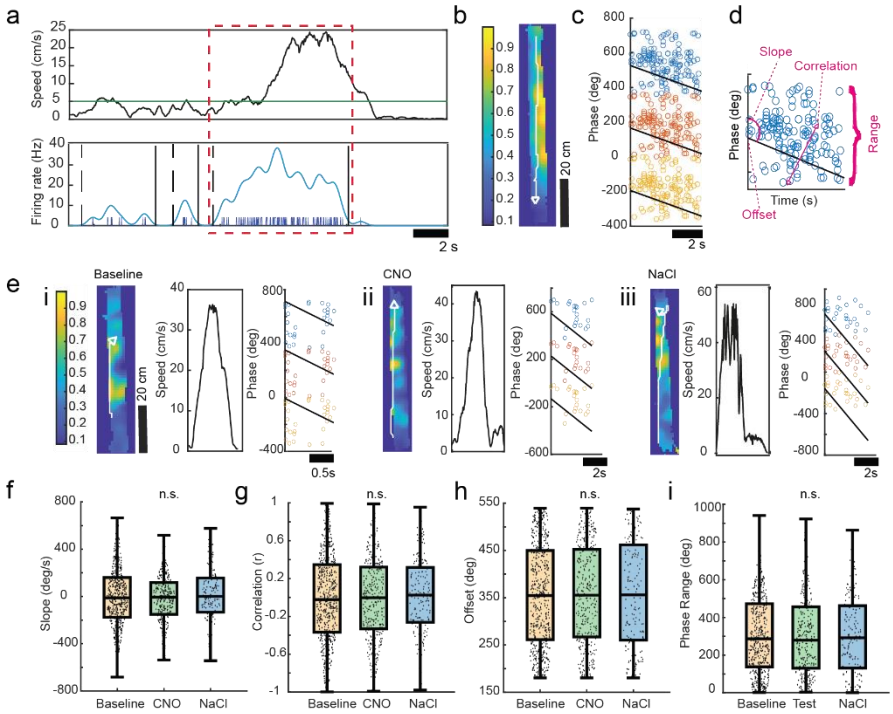

Figure 7. Comparison of phase precession between baseline, CNO and NaCl sessions

(A) Top: Example trace of 20 s of an animal's speed (cm/s). Green horizontal line represents 5 cm/s cutoff for average speed for phase precession (PP) epochs. Bottom: Firing rate of a putative pyramidal cell from the same 20s shown in (A). Dark blue ticks indicate spikes, with the pale blue trace showing extrapolated spiking rate after convolution with a Gaussian curve. Dotted and solid black vertical lines show beginning and end of putative epochs of PP. Box with red dotted lines indicates example epoch shown in B-C. **(B)** Trajectory of mouse during example epoch superimposed on normalized rate map from recording. **(C)** Spikes from example epoch plotted as a function of time (x axis) and phase (y axis). The black line represents the line of best fit from circular-linear regression. Note: the same putative epoch of PP is plotted here three times in blue, orange and yellow to aid visualization. **(D)** Schematic of calculation of parameters related to quality of PP drawn from spikes plotted as a function of time and phase as in (C). **(E)** Example PP epochs from baseline (i), CNO (ii), and NaCl recordings (iii). Each subpanel shows the mouse's trajectory (white) superimposed on a rate map for the recording (left), speed (middle) and spikes plotted as a function of time (x axis) and phase (y axis). The 3 examples shown here are from 3 different mice and recording days. **(F)** Comparison of PP slope (deg/s) in baseline (yellow, left), CNO (green, middle) and NaCl recordings (blue, right). **(G)** Comparison of circular correlation values (r) in baseline (yellow, left), CNO (green, middle) and NaCl recordings (blue, right). *(Figure legend continues on next page*)

(H) Comparison of phase offset (deg) in baseline (yellow, left), CNO (green, middle) and NaCl recordings (blue, right). **(I)** Comparison of phase range (deg) in baseline (yellow, left), CNO (green, middle) and NaCl recordings (blue, right). For all box plots in this figure: Horizontal black lines indicate group medians, with box edges delineating 25th and 75th percentiles. Box whiskers extend to most extreme data points. N = 474, 297, and 173 PP epochs from 4 mice. N.s. = not significant at $p > 0.05$. *Original figure.*

As with slope, there was also no significant difference between circular-linear correlation values, phase offset or phase range between baseline, CNO and NaCl sessions (**Figure 7g**: Correlation: baseline = -0.021 ± 0.72, CNO = - 0.0028 ± 0.65, NaCl = 0.025 ± 0.58; $p = 0.75$, $H(2) = 0.58$; **Figure 7h**: Phase offset: baseline = -0.021 ± 0.72, CNO = - 0.0028 ± 0.65, NaCl = 0.025 ± 0.58; $p = 0.75$, $H(2) = 0.58$; **Figure 7i**: Phase range: baseline = 470.16 ± 334.43 deg, CNO = 458.19 ± 325.24 deg, NaCl = 471.07 ± 330.14 deg; $p = 0.81$, $H(2) = 0.43$, Kruskal-Wallis test, n = 474 (baseline), 297 (CNO) and 173 (NaCl) runs from 4 mice). Thus, silencing L3PCs does not appear to have an effect on PP in CA1.

While PP was largely unaffected by CNO treatment of L3PCs, it is possible that these cells play a role in other aspects of spatial coding. Thus, I compared the several measures of CA1 place cell activity between baseline, CNO, and NaCl recordings. Place fields were present in all 3 recording conditions, and showed high stability between baseline and test (CNO or NaCl) conditions (**Figure 8a**). The proportions of cells with 0, 1 or 2+ fields did not differ between the three recording conditions (**Figure 8b**: $p = 0.68$, $X^2(4) = 2.29$, Chi Square test, n = 37, 24 and 13 cells from 4 mice).

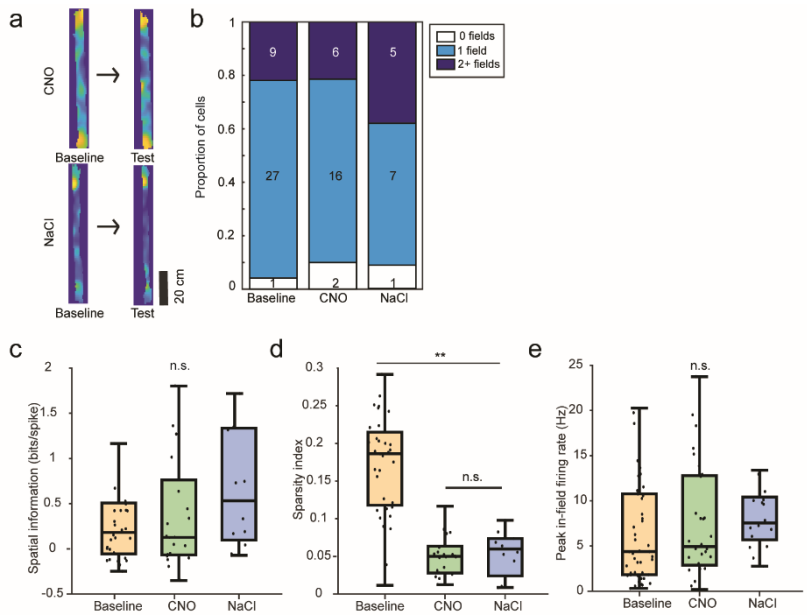

Figure 8: Comparison of spatial firing in baseline, CNO and NaCl recordings

(A) Example of rate maps from baseline (left) and test recordings (right) approximately 1 hour after injection of CNO (top) or NaCl (bottom). **(B)** Comparison of the proportion of putative pyramidal cells with 0 (white), 1 (pale blue) and 2+ (dark blue) place fields. Text inset indicates the number of cells in each category. **(C)** Comparison of spatial information (bits/spike) in baseline (yellow, left), CNO (green, middle) and NaCl recordings (blue, right). N = 37, 24 and 13 cells from 4 mice. **(D)** Comparison of spatial sparsity index in baseline (yellow, left), CNO (green, middle) and NaCl recordings (blue, right). N = 37, 24 and 13 cells from 4 mice. **(E)** Comparison of peak in-field firing (Hz) in baseline (yellow, left), CNO (green, middle) and NaCl recordings (blue, right). N = 46, 29 and 17 place fields from 4 mice. For all box plots in this figure: Horizontal black lines indicate group medians, with box edges delineating 25th and 75th percentiles. Box whiskers extend to most extreme data points. * = significant at $p < 0.05$, n.s. = not significant at $p > 0.05$. *Original figure.*

Next, I examined whether the spatial information of CA1 PCs differed between conditions. Here, there was also no statistically significant difference between groups (**Figure 8c**: baseline = 0.18 ± 0.58 bits/spike, CNO = 0.13 ± 0.65 bits/spike, NaCl = 0.33 ± 1.31 bits/spike, $H(2) = 1.48$, $p = 0.48$, Kruskal-Wallis test). I also compared the spatial sparsity index, a representation of the fraction of the recording arena in which a given cell is active[52]. Here, there was a substantial difference between groups (**Figure 8d,** baseline sparsity index = 0.19 ± 0.093, CNO sparsity index = 0.050 ± 0.032, NaCl sparsity index = 0.064 ± 0.038; $p < 0.001$, $H(2) = 43.06$, Kruskal-Wallis test, n = 37, 24 and 13 cells from 4 mice), which was ascribable to differences between CNO and baseline ($p < 0.0001$) and NaCl and baseline sessions ($p < 0.0001$), but not between CNO and NaCl ($p = 0.96$, Dunn's multiple comparison test). Thus it appears to be a non-specific effect. Finally, to assess whether spatial firing was disturbed on the level of individual place fields, the peak in-field firing between place fields in all three groups. No difference was detected (**Figure 8e**: baseline = 4.38 ± 8.93, CNO = 5.18 ± 9.84, NaCl = 7.84 ± 4.55; $p = 0.16$, $H(2) = 3.70$; Kruskal-Wallis test, n = 46, 29 and 17 fields from 4 mice). To summarize, silencing L3PC projections with CNO had no effect on either PP or spatial coding of place cells in measured in CA1.

6. Discussion and Limitations

6.1 Role of L3PCs in up down state experiments

The first part of this thesis explored the role of L3PCs in US in the MEC. I found that, akin to previous studies *in vitro*[39,40] and *in vivo*[44,45], L3 was highly active in an anaesthetized model, and that the frequency and duration of detected US remained steady over time (**Figure 1d**). This provided an ideal framework for studying different properties of US in a controlled manner. To this end, I used a mouse line with constitutive expression of Arch in L3PCs to silence US using optogenetic tools. A pulse barrage protocol indeed succeeded in dramatically reducing the frequency of US, while leaving their duration intact (**Figure 2b**). Therefore, I took recourse to a closed-loop system, where an LED was fired in response to first deflections of the LFP, allowing for more time-locked control of L3PC activity (**Figure 4a**). Here, effects on the frequency of US were slightly weaker (**Figure 4d**), suggesting that inhibition of L3PC activity after US were already initiated was less successful at suppressing future US. The transition between Down state to US is thought to be mediated by thalamic drive (although see isolated slice experiments in Beed, De Filippo, Holman et al., 2020[79]), and through a complex interplay of excitation and inhibition[8,40]. Thus, US may already have been "in progress" at the onset of the light stimulation, such that the US could not be silenced as effectively via inhibition of L3PCs.

While it is known that US propagate to deep layers of the MEC, it is not clear whether this is due to activity propagated by L2SCs or L3PCs, though L3PCs are strongly suggested by *in vitro* experiments (Beed, De Filippo Holman et al., 2020[79]). Could interrupting the activity of L2SCs, which are downstream of L3PCs[28] "break" the chain of propagation and substantially alter US properties? Here, using NpHR virally expressed in the L2SC-specific Uchl1-Cre line, we found that this was not the case (**Figure 4a-d**). Thus it seems that L2SCs likely receive excitatory US-related input from L3PCs, but that their activity was not crucial for initiating or controlling duration of US. However, one limitation of these experiments is the matter of genetic versus viral expression of optogenetic proteins in different mouse lines used for these experiments[82]. A more direct comparison across would entail either implementing a completely genetic strategy (e.g. crossing the Uchl1-Cre with the Ai40D line for higher expression levels), or performing follow-up experiments with Oxr1-Cre mice and viral expression of NpHR. However, control experiments with closed-loop stimulation in WT mice do seem to rule out systemic confounds, such as off-target effects from tissue heating from optogenetic stimulation (**Figure 4e-h**, see also[83]). Overall,

a contrast between all 3 lines used in this study highlights a special role of L3PCs in the initiation of US in the MEC (**Figure 4i**).

Generally, there are still some global limitations to studying US using the model chosen here. First, while it is known that anaesthesia replicates many features of UDS in sleeping mice[45,84,85], it can dramatically alter signal integration and cortico-thalamic coupling[86]. This could mean that anaesthesia leads to more homogenous, less complex cortical activity compared to sleep or awake preparations[87,88]. Urethane, in particular, activates a wide range of neurotransmitter-gated ion channels, and it is difficult to elucidate all of its effects on a cellular level[89]. Thus it is important to determine whether these US findings still hold true in a non-anaesthetized state.

6.2 Role of L3PCs in phase precession and spatial coding

In the second group of experiments in this thesis, I explored the role of L3PCs in spatial coding in CA1, particularly, PP. While silencing of cells of projections from L3PCs in *in vitro* experiments with hM4D was successful (data not shown), findings from *in vivo* experiments do not support a large role for L3PCs in spatial coding in CA1 (**Figures 5-8**). Here, I found that CA1 PCs appeared to undergo a slight increase in firing rate in the presence of CNO (**Figure 6a**), whereas there was no effect in INs (**Figure 6b**). Measures of average running speed running also did not point to a large effect of the drug (**Figure 6c**). The use of DREADDs in neuroscience has previously raised concerns about the exact mechanism of CNO action and off-target effects[80,90]. Two experimental approaches could help clarify and contextualize results of my study in the future. First, one could attempt continuous recordings at L3PC projections in CA1 directly after injection (mice in this study had a 1 hour break between baseline and test sessions). This could help verify whether the synaptic effects seen *in vitro* are also present *in vivo*, or whether synaptic drive from other regions such as CA3 is ramped up in response to silencing of L3PC projections. Second, if the effectiveness of CNO was limited by low infection rates of L3PCs, one could consider switching to a genetically-driven hM4D approach (as with Oxr1 x Ai40D crosses, above). This could potentially improve receptor expression and effect magnitude, although appropriate controls of genetic expression are still necessary[91]. Infusion of CNO directly into CA1 could also reduce potential off-target effects, but was not attempted here due to the size of the 32-channel chronic implant.

In the main body of experiments, I used these data to explore the effects of L3PCs on PP in area CA1 (**Figure 7**). Contrary to the initial hypothesis, and predictions from both theoretical[56] and

experimental[51,54] studies, I found that the slope, circular-linear correlation, phase offset and phase range were virtually identical between baseline, CNO and NaCl recordings (**Figure 7f-i**). This could imply that PP could be generated locally, perhaps via dendritic mechanisms[92], in CA1, or somewhere along the indirect path, such as short-term facilitation at mossy fiber synapses in CA3[93]. Alternative explanations with respect to alternate pathways and network models of PP are also discussed below.

However, it is first important to consider analytical limitations of PP experiments. Here, for analyzing PP I used a method adopted from Aghajan et al.[72], as it has been shown to detect more spikes than standard methods of PP analysis (which use place fields defined *a priori*), particularly when spatial firing is sparse or irregular[72,73]. An important future line of analysis would be to compare both analysis strategies, and see which more accurately captures patterning of temporal activity of CA1 PC spikes.

In addition to measures of PP, I also examined the impact of silencing L3PC projections on place cells in CA1. In line with previous papers on L3PC silencing[32,33], I could not identify major changes in the spatial information, sparsity or peak in-field firing of CA1 PCs (**Figure 8a-e**). The finding on in-field firing is interesting, especially given the slight overall increase in firing rate after CNO application (note: the ratio of in-field/out-field firing rates was also unaltered [data not shown]). This suggest that any CNO-induced alterations were not strong or specific enough to substantially impact spatial coding in this study. Interestingly, Bittner and colleagues[47] found that optogenetic silencing of L3PC projections in CA1 only resulted in subtle changes to dendritic membrane potential, related to place cell formation, measured by whole cell patch clamp. If a similar effect was present in my data, it was not detectable at the level of extracellular waveform sorting.

Taken together, these findings suggest that chemogenetic silencing of L3PC projections are not sufficient to substantially alter PP or spatial coding in area CA1. This has several implications, particularly for network models of PP. First, it strongly suggests that alterations to PP in studies silencing the MEC in a non-cell-specific manner[30,36] were at least partially by cell populations other than L3PCs. Two immediate candidates are L2SCs (exerting influence in CA1 via the dentate gyrus, CA3, and the indirect pathway – though note weak PP in L2SCs noted in ref[94]), and cells in CA3 themselves[88]. Second, these findings imply that inheritance from L3PCs cannot explain all features of PP in area CA1 as predicted by variations of some models[56]. Indeed the possible

importance of projections from CA3 for PP in CA1 has been highlighted by several theoretical network models and experimental reports[57,95,96]. However, recent experimental work showing intact PP in CA1 after silencing CA3[60] also counters this hypothesis, although concurrent changes to place cell properties in the study make this finding difficult to interpret.

Ultimately, it is likely that PP and spatial coding in CA1 are the result of complex interplay between projections from the MEC and CA3. This may include contributions at the of level cell- and layer-specific inputs[51,54,57,96]. Further stratifying my data by exact recording depth (i.e. predominantly L3PC or CA3 input sublayers) might bring more subtle effects to light (e.g. identifying deep pyramidal cells by anatomy and electrophsyiological properties[51]). Alternatively, one could perform recordings deep in the *striatum lacunosum moleculare* of CA1, where projections from L3PCs enter the hippocampus to pick up on subtle dendritic effects or activity of layer-specific INs[3]. A dissociation between CA3 and L3PCs could also be highlighted in behavioral tasks other than navigation, such as those including novel environments[51,54].

7. Outlook

The work in this thesis has explored the role of L3PCs in the MEC in two seemingly contrasting areas: slow oscillations in a model of sleep, and spatial coding during active exploration. The first set of experiments points to a direct role of L3PCs in the local generation and maintenance of US. The second set of experiments show that L3PCs did not play a crucial role in spatial coding in CA1, perhaps working instead in conjunction with contributions from other projections. These two experimental directions are united by several important themes which could be crucial for future work.

7.1 Outstanding questions on connectivity

Despite being at the focus on research on learning and memory for decades, there is much that is still unknown about connectivity in the HC and MEC. For example, MEC L5b receives input from both L2SCs and L3PCs[64,65], as well as the hippocampus[64,97], allowing it to potentially act as a coincidence detector during US[65] (see also Beed, De Filippo, Holman et al., 2020[79]). However, a recent study has called this intra-MEC connectivity into question[98] Thus, a better understanding of intra-MEC connectivity during slow oscillations could complement existing studies *in vitro* [28,29], and provide clues about how activity from L3PCs is propagated to other brain regions in a variety of contexts, including navigation.

Similarly, connectivity between L3PCs and area CA1 is still very much under investigation. It is not clear to what extent L3PCs synapse directly onto CA1 pyramids, or interneurons. The increased firing rate of PCs after L3PC inhibition (**Figure 6a**) suggests a role for feedforward disinhibition. However, at a population level a decrease in interneuron firing could not be confirmed (**Figure 6b**), Here, more connectivity studies using cell-type specific mouse lines (see for example Bittner et al.[47], Suppl. Figure 8, showing ChR2-assisted connectivity mapping) are warranted. Furthermore, recent works have also illuminated the role of "non-canonical" HC inputs in area CA1, such as L2 pyramidal cells from the MEC[99], or projections from L3PCs to the subiculum[100]. Once again, gaining a better understanding of which projections are active when could provide powerful clues for understanding HC-MEC synchronization during US[44,45], or integration of different types of spatial information during navigation[101].

7.2 L3PCs in behavior and pathology

In this thesis, I sought to explore the role of L3PCs in two different conditions: slow oscillations and navigation. However, there is growing evidence that suggest that these cells may play a role in other forms of behavior. For example, Yamamoto and Tonegawa[33] found that silencing L3PCs led to more fragmented spatial replay, which they correlated with earlier work describing L3-induced deficits in tasks requiring a temporal delay[32,46]. Reports of US *in vivo* have noted that L3PCs' persistent activity may allow them to bias activity of the HC and cortex on the timescale of seconds, potentially aiding in "interleaving" neocortical and hippocampal activity[45,102,103]. Thus L3PCs' may be more important for gating temporal control of HC-MEC than providing direct (spatial) information to CA1[101], and may be best illuminated by tasks that require fine temporal discrimination. Other authors have suggested that L3PCs activity is most prominent during exposure to novel contexts[51,54], yet this has yet to be tested causally. Silencing approaches found in this thesis could be adapted to more sophisticated behavioral tasks, as task complexity has also been shown to amplify the spatial information coded-for by place cells[104]. These tasks could be helpful in distinguishing whether L3PCs are most important for "online" processing of (spatial) information, or more critical for memory consolidation during sleep and slow oscillations thereafter.

It is well established that the MEC is a site of early neurodegeneration in conditions such as Alzheimer's disease and epilepsy[5–7], particularly in L3[105,106]. In the case of slow waves, it has previously been shown that coordination between the HC and cortex can be disrupted by amyloid-

β plaques[13], or interictal epileptiform discharges[14], correlating in both cases with memory impairment. While understanding the underlying cellular pathology in L3 is outside the scope of this work, developing paradigms complementary to the ones used in this paper might provide an opportunity to boost HC-MEC communication and bolster memory, for example, as shown by a study augmenting slow wave activity in healthy young adults[107].

Great strides have also recently been made in aligning human and rodent studies on navigation and functional cell types in the hippocampal system[108,109], including efforts to align observed pathology with functional deficits on a cellular or network basis in rodent models[110,111]. The presence of navigational difficulties in the early stages of AD or mild cognitive impairment are also gaining recognition[112]. More refined and non-invasive diagnostic or experimental techniques in humans, ideally involving celltype- or layer-specific connectivity[113,114], may be able to provide a more definitive link between L3PC pathology and symptoms of neurodegenerative disorders. One day, detection of fine alterations in these cells or their projections may inform pre-symptomatic diagnostic biomarkers.

8. Conclusion

Communication between the HC and MEC is crucial in a variety of cognitive functions, and advances in cell-specific mouse lines and recording techniques mean that inter-regional projections and synchrony can be explored with high levels of precision. In this work, I studied to role of L3PCs in the MEC in both UDS and their contribution to place cells in CA1 during navigation. While these cells appear to play an important role in slow oscillations, their importance for spatial coding and PP remains to be elucidated. These findings add to the growing body of literature of layer- and cell-type specific contributions to network activity in the hippocampal network, and suggest future avenues of investigation with respect to both physiological and pathological activities in these structures.

9. Works Cited

1. Buzsáki G. *Rhythms of the Brain*.; 2009. doi:10.1093/acprof:oso/9780195301069.001.0001
2. Buzsaki G, Moser EI. Memory, navigation and theta rhythm in the hippocampal- entorhinal system. *Nat Neurosci*. 2013;16(2):130-138. doi:10.1038/nature13314.A
3. Valero M, de la Prida LM. The hippocampus in depth: a sublayer-specific perspective of entorhinal–hippocampal function. *Curr Opin Neurobiol*. 2018;52:107-114. doi:10.1016/j.conb.2018.04.013
4. Canto CB, Wouterlood FG, Witter MP. What does the anatomical organization of the entorhinal cortex tell us? *Neural Plast*. 2008;2008. doi:10.1155/2008/381243
5. Huijbers W, Mormino EC, Wigman, SE, Ward AM, Vannini, P, McLaren DG, Becker JA, Schultz AP, Hedden T, Johnson KA, Sperling RA. Amyloid Deposition Is Linked to Aberrant Entorhinal Activity among Cognitively Normal Older Adults. *J Neurosci*. 2014;34(15):5200-5210. doi:10.1523/JNEUROSCI.3579-13.2014
6. Stranahan AM, Mattson MP. Selective vulnerability of neurons in layer II of the entorhinal cortex during aging and Alzheimer's disease. *Neural Plast*. 2010;2010. doi:10.1155/2010/108190
7. Vismer MS, Forcelli PA, Skopin MD, Gale K, Koubeissi MZ. The piriform, perirhinal, and entorhinal cortex in seizure generation. *Front Neural Circuits*. 2015;9(May):1-14. doi:10.3389/fncir.2015.00027
8. Neske GT. The slow oscillation in cortical and thalamic networks: Mechanisms and functions. *Front Neural Circuits*. 2016;9(JAN2016):1-25. doi:10.3389/fncir.2015.00088
9. Tukker JJ, Beed P, Schmitz D, Larkum ME, Sachdev RNS. Up and Down States and Memory Consolidation Across Somatosensory, Entorhinal, and Hippocampal Cortices. *Front Syst Neurosci*. 2020;14:1-35. doi:10.3389/fnsys.2020.00022
10. Colgin LL. Theta-gamma coupling in the entorhinal-hippocampal system. *Curr Opin Neurobiol*. 2015;31:45-50. doi:10.1016/j.conb.2014.08.001
11. Hasselmo ME, Stern CE. Theta rhythm and the encoding and retrieval of space and time. *Neuroimage*. 2015;85(0 2):656-666. doi:10.1016/j.neuroimage.2013.06.022.Theta
12. Buzsáki G. Theta oscillations in the hippocampus. *Neuron*. 2002;33(3):325-340. papers3://publication/uuid/90B140FB-AC03-4F7C-9968-EF84D84A3009.
13. Mander BA, Marks SM, Vogel JW, Rao V, Lu B, Saletin JM, Ancoli-Israle S, Jagust WJ, Walker MP. β-amyloid disrupts human NREM slow waves and related hippocampus-dependent memory consolidation. *Nat Neurosci*. 2015;18(7):1051-1057.

doi:10.1038/nn.4035

14. Gelinas JN, Khodagholy D, Thesen T, Devinsky O, Buzsáki G. Interictal epileptiform discharges induce hippocampal-cortical coupling in temporal lobe epilepsy. *Nat Med*. 2016;22(6):641-648. doi:10.1038/nm.4084
15. Steward O, Scoville SA. Cells of origin of entorhinal cortical afferents to the hippocampus and fascia dentata of the rat. *J Comp Neurol*. 1976;169(3):347-370. doi:10.1002/cne.901690306
16. Hafting T, Fyhn M, Molden S, Moser MB, Moser EI. Microstructure of a spatial map in the entorhinal cortex. *Nature*. 2005;436(7052):801-806. doi:10.1038/nature03721
17. Zhang SJ, Ye J, Miao C, Tsao A, Cerniauskas I, Lederberber D, Moser MB, Moser EI. Optogenetic dissection of entorhinal-hippocampal functional connectivity. *Science (80-).* 2013;340(6128):44. doi:10.1126/science.1232627
18. Germroth P, Schwerdtfeger WK, Buhl EH. Morphology of Identified Neurons Projecting To the Hippocampus . a Light Study Combining Retrograde Tracing and Intracellular. *Neuroscience*. 1989;30(3):683-691.
19. Dickson CT, Mena AR, Alonso A. Electroresponsiveness of medial entorhinal cortex layer III neurons in vitro. *Neuroscience*. 1997;81(4):937-950. doi:10.1016/S0306-4522(97)00263-7
20. Gloveli T, Schmitz D, Empson RM, Dugladze T, Heineman U. Morphological and Electrophysiological Characterization of Layer III Cells of the Medial Entorhinal Cortex of the Rat. *Neuroscience*. 1997;(3):629-648.
21. van der Linden S, Lopes da Silva FH. Comparison of the electrophysiology and morphology of layers III and II neurons of the rat medial entorhinal cortex in vitro. *Eur J Neurosci*. 1998;10(4):1479-1489. doi:10.1046/j.1460-9568.1998.00162.x
22. Hafting T, Fyhn M, Bonnevie T, Moser M, Moser EI. Hippocampus-independent phase precession in entorhinal grid cells. *Nature*. 2008;453(7489):1248-1253. doi:10.1038/nature06957
23. Sargolini F, Fyhn M, Hafting T, McNaughton BL, Witter MP, Moser MB, Moser EI. Conjunctive representation of position, direction, and velocity in entorhinal cortex. *Science (80-).* 2006;312(5774):758-762. doi:10.1126/science.1125572
24. Tang Q, Ebbesen CL, Sanguinetti-Scheck JI, Preston-Ferrer P, Gundlfinger A, Winterer J, Beed P, Ray S, Naumann R, Schmitz D, Brecht M, Burgalossi A. Anatomical Organization and Spatiotemporal Firing Patterns of Layer 3 Neurons in the Rat Medial Entorhinal Cortex. *J Neurosci*. 2015;35(36):12346-12354. doi:10.1523/JNEUROSCI.0696-15.2015

25. Burgalossi A, Herfst L, von Heimendahl M, Först H, Haskic K, Schmidt M, Brecht M. Microcircuits of Functionally Identified Neurons in the Rat Medial Entorhinal Cortex. *Neuron*. 2011;70(4):773-786. doi:10.1016/j.neuron.2011.04.003
26. Mizuseki K, Sirota A, Pastalkova E, Buzsáki G. Theta Oscillations Provide Temporal Windows for Local Circuit Computation in the Entorhinal-Hippocampal Loop. *Neuron*. 2009;64(2):267-280. doi:10.1016/j.neuron.2009.08.037
27. Quilichini P, Sirota A, Buzsáki G. Intrinsic circuit organization and theta-gamma oscillation dynamics in the entorhinal cortex of the rat. *J Neurosci*. 2011;30(33):11128-11142. doi:10.1016/j.str.2010.08.012.Structure
28. Winterer J, Maier N, Wozny C, Beed P, Breustedt J, Evangelista R, Peng Y, D'Albis T, Kempter R, Schmitz D. Excitatory Microcircuits within Superficial Layers of the Medial Entorhinal Cortex. *Cell Rep*. 2017;19(6):1110-1116. doi:10.1016/j.celrep.2017.04.041
29. Couey JJ, Witoelar A, Zhang SJ, Zheng K, Ye J, Dunn B, Czakowski R, Moser MB, Moser EI, Roudi Y, Witter MP. Recurrent inhibitory circuitry as a mechanism for grid formation. *Nat Neurosci*. 2013;16(3):318-324. doi:10.1038/nn.3310
30. Ormond J, McNaughton BL. Place field expansion after focal MEC inactivations is consistent with loss of Fourier components and path integrator gain reduction. *Proc Natl Acad Sci*. 2015;112(13):4116-4121. doi:10.1073/pnas.1421963112
31. Hales JB, Schlesiger MI, Leutgeb JK, Squire LR, Leutgeb S, Clark RE. Medial entorhinal cortex lesions only partially disrupt hippocampal place cells and hippocampus- dependent place memory. *Cell Rep*. 2014;9(3):893-901. doi:10.1016/j.celrep.2014.10.009
32. Yamamoto J, Suh J, Takeuchi D, Tonegawa S. Successful Execution of Working Memory Linked to Synchronized High-Frequency Gamma Oscillations. *Cell*. 2014;157(4):845-857. doi:10.1016/j.cell.2014.04.009
33. Yamamoto J, Tonegawa S. Direct Medial Entorhinal Cortex Input to Hippocampal CA1 Is Crucial for Extended Quiet Article Direct Medial Entorhinal Cortex Input to Hippocampal CA1 Is Crucial for Extended Quiet Awake Replay. *Neuron*. 2017;96(1):217-227.e4. doi:10.1016/j.neuron.2017.09.017
34. Brun VH, Leutgeb S, Wu HQ, Schwarcz R, Witter MP, Moser EI, Moser MB. Impaired Spatial Representation in CA1 after Lesion of Direct Input from Entorhinal Cortex. *Neuron*. 2008;57(2):290-302. doi:10.1016/j.neuron.2007.11.034
35. Robinson J, Manseau F, Ducharme G, Amilhon B, Vigneault E, El Mestikawy S, Williams S. Optogenetic Activation of Septal Glutamatergic Neurons Drive Hippocampal Theta Rhythms. *J Neurosci*. 2016;36(10):3016-3023. doi:10.1523/JNEUROSCI.2141-15.2016

36. Schlesiger MI, Cannova CC, Boublil BL, Hales JB, Mankin EA, Brandon MP, Leutgeb JK, Leibold C, Leutgeb S. The medial entorhinal cortex is necessary for temporal organization of hippocampal neuronal activity. *Nat Neurosci*. 2015;18(8):1123-1132. doi:10.1038/nn.4056

37. Massimini M, Ferrarelli F, Huber R, Esser SK, Singh H, Tononi G. Neuroscience: Breakdown of cortical effective connectivity during sleep. *Science (80-).* 2005;309(5744):2228-2232. doi:10.1126/science.1117256

38. Luczak A, Barthó P, Marguet SL, Buzsáki G, Harris KD. Sequential structure of neocortical spontaneous activity in vivo. *Proc Natl Acad Sci U S A*. 2007;104(1):347-352. doi:10.1073/pnas.0605643104

39. Tahvildari B, Wölfel M, Duque A, McCormick DA. Selective functional interactions between excitatory and inhibitory cortical neurons and differential contribution to persistent activity of the slow oscillation. *J Neurosci*. 2012;32(35):12165-12179. doi:10.1523/JNEUROSCI.1181-12.2012

40. Mann EO, Kohl MM, Paulsen O. Distinct roles of GABAA and GABAB receptors in balancing and terminating persistent cortical activity. *J Neurosci*. 2009;29(23):7513-7518. doi:10.1523/JNEUROSCI.6162-08.2009

41. Bartram J, Kahn MC, Tuohy S, Paulsen O, Wilson T, Mann EO. Cortical Up states induce the selective weakening of subthreshold synaptic inputs. *Nat Commun*. 2017;8(1). doi:10.1038/s41467-017-00748-5

42. Kim J, Gulati T, Ganguly K. Competing Roles of Slow Oscillations and Delta Waves in Memory Consolidation versus Forgetting. *Cell*. 2019;179(2):514-526.e13. doi:10.1016/j.cell.2019.08.040

43. Cunningham MO, Pervouchine DD, Racca C, Kopell NJ, Davies CH, Jones RSG, TRaub RD, Whittington MA. Neuronal metabolism governs cortical network response state. *Proc Natl Acad Sci U S A*. 2006;103(14):5597-5601. doi:10.1073/pnas.0600604103

44. Isomura Y, Sirota A, Özen S, Montgomery S, Mizuseki K, Henze DA, Buzsaki G . Integration and Segregation of Activity in Entorhinal-Hippocampal Subregions by Neocortical Slow Oscillations. *Neuron*. 2006;52(5):871-882. doi:10.1016/j.neuron.2006.10.023

45. Hahn TTG, Mcfarland JM, Berberich S, Sakmann B, Mehta MR. Spontaneous persistent activity in entorhinal cortex modulates cortico-hippocampal interaction in vivo. *Nat Neurosci*. 2012;15(11):1531-1538. doi:10.1038/nn.3236

46. Suh J, Rivest AJ, Nakashiba T, Tominaga T, Tonegawa S. Entorhinal Cortex Layer III Input

to the Hippocampus Is Crucial for Temporal Association Memory. *Science (80-).* 2011;334:1415-1421. doi:10.1126/science.1210125

47. Bittner KC, Grienberger C, Vaidya SP, Milstein AD, Macklin JJ, Suh J, Tonegawa S, Magee JC. Conjunctive input processing drives feature selectivity in hippocampal CA1 neurons. *Nat Neurosci*. 2015;18(8):1133-1142. doi:10.1038/nn.4062
48. O'Keefe J, Recce ML. Phase Relationship Between Hippocampal Place Units and the EEG Theta Rhythm. *Hippocampus*. 1993;3(3):317-330. doi:10.1016/j.neuron.2015.09.051
49. Jensen O, Lisman JE. Position reconstruction from an ensemble of hippocampal place cells: Contribution of theta phase coding. *J Neurophysiol*. 2000;83(5):2602-2609. doi:10.1152/jn.2000.83.5.2602
50. Reifenstein ET, Kempter R, Schreiber S, Stemmler MB, Herz AVM. Grid cells in rat entorhinal cortex encode physical space with independent firing fields and phase precession at the single-trial level. *Proc Natl Acad Sci U S A*. 2012;109(16):6301-6306. doi:10.1073/pnas.1109599109
51. Sharif F, Tayebi B, Buzsáki G, Royer S, Fernandez-Ruiz A. Subcircuits of Deep and Superficial CA1 Place Cells Support Efficient Spatial Coding across Heterogeneous Environments. *Neuron*. 2021;109(2):363-376.e6. doi:10.1016/j.neuron.2020.10.034
52. Skaggs WE, McNaughton BL, Wilson MA, Barnes CA. Theta phase precession in hippocampal neuronal populations and the compression of temporal sequences. *Hippocampus*. 1996;6(2):149-172. doi:10.1002/(SICI)1098-1063(1996)6:2<149::AID-HIPO6>3.0.CO;2-K
53. Reifenstein ET, Kempter R. Synaptic learning rules for sequence learning. *bioRxiv*. 2020:1-28. doi:10.1101/2020.04.13.039826
54. Fernández-Ruiz A, Oliva A, Nagy G, Maurer AP, Berenyi A, Buzsáki G. Entorhinal-CA3 Dual-Input Control of Spike Timing in the Hippocampus by Theta-Gamma Coupling. *Neuron*. 2017;93(5):1213-1226.e5. doi:10.1016/j.neuron.2017.02.017
55. Mizuseki K, Diba K, Pastalkova E, Buzsáki G. Hippocampal CA1 pyramidal cells form functionally distinct sublayers. *Nat Neur*. 2011;14(9):1174-1181. doi:10.1016/j.physbeh.2017.03.040
56. Jaramillo J, Schmidt R, Kempter R. Modeling inheritance of phase precession in the hippocampal formation. *J Neurosci*. 2014;34(22):7715-7731. doi:10.1523/JNEUROSCI.5136-13.2014
57. Chance FS. Hippocampal phase precession from dual input components. *J Neurosci*. 2012;32(47):16693-16703. doi:10.1523/JNEUROSCI.2786-12.2012

58. Zutshi I, Brandon MP, Fu ML, Donegan ML, Leutgeb JK, Leutgeb S. Hippocampal Neural Circuits Respond to Optogenetic Pacing of Theta Frequencies by Article Hippocampal Neural Circuits Respond to Optogenetic Pacing of Theta Frequencies by Generating Accelerated Oscillation Frequencies. *Curr Biol*. 2018;28(8):1179-1188.e3. doi:10.1016/j.cub.2018.02.061

59. Climer JR, Newman EL, Hasselmo ME. Phase Coding By Grid Cells In Unconstrained Environments: Two-Dimensional Phase Precession. *Eur J Neurosci*. 2013;38(4):2526-2541. doi:10.1111/ejn.12256

60. Davoudi H, Foster DJ. Acute silencing of hippocampal CA3 reveals a dominant role in place field responses. *Nat Neurosci*. 2019;22(3):337-342. doi:10.1038/s41593-018-0321-z

61. Fuchs EC, Neitz A, Pinna R, Melzer S, Caputi A, Monyer H. Local and Distant Input Controlling Excitation in Layer II of the Medial Entorhinal Cortex. *Neuron*. 2016;89(1):194-208. doi:10.1016/j.neuron.2015.11.029

62. Roth BL. DREADDs for Neuroscientists. *Neuron*. 2016;89(4):683-694. doi:10.1016/j.neuron.2016.01.040

63. Wozny C, Beed P, Nitzan N, Pössnecker Y, Rost BR, Schmitz D. VGLUT2 functions as a differential marker for hippocampal output neurons. *Front Cell Neurosci*. 2018;12(October):1-5. doi:10.3389/fncel.2018.00337

64. Sürmeli G, Marcu DC, Mcclure C, Garden DLF, Pastoll H, Nolan MF. Molecularly Defined Circuitry Reveals Input-Output Segregation in Deep Layers of the Medial Entorhinal Article Molecularly Defined Circuitry Reveals Input-Output Segregation in Deep Layers of the Medial Entorhinal Cortex. *Neuron*. 2015;88:1040-1053. doi:10.1016/j.neuron.2015.10.041

65. Ohara S, Onodera M, Simonsen ØW, Yoshino R, Hioki H, Iijima T, Tsutsui KI, Witter MP. Intrinsic Projections of Layer Vb Neurons to Layers Va , III , and II in the Lateral and Medial Entorhinal Cortex of the Rat Article Intrinsic Projections of Layer Vb Neurons to Layers Va , III , and II in the Lateral and Medial Entorhinal Cortex of the R. *CellReports*. 2018;24(1):107-116. doi:10.1016/j.celrep.2018.06.014

66. Lopes G, Bonacchi N, Frazão J, Neto JP, Atallah BV, Soares S, Moreira L, Matias S, Itskov PM, Correia PA, Medina RE, Calcaterra L, Dreosti E, Paton JJ Kampff AR. Bonsai: An event-based framework for processing and controlling data streams. *Front Neuroinform*. 2015;9(APR):1-14. doi:10.3389/fninf.2015.00007

67. Seamari Y, Narváez JA, Vico FJ, Lobo D, Sanchez-Vives M V. Robust off- and online separation of intracellularly recorded up and down cortical states. *PLoS One*. 2007;2(9).

doi:10.1371/journal.pone.0000888

68. Pachitariu M, Steinmetz N, Kadir S, Carandini M, Harris K. Fast and accurate spike sorting of high-channel count probes with KiloSort. *Adv Neural Inf Process Syst*. 2016;(Nips):4455-4463.
69. Stockwell RG, Mansinha L, Lowe RP. Localization of the complex spectrum : the S transform. *IEEE Trans Signal Process*. 1996;44(May):993. papers3://publication/uuid/4EB9094B-305F-48BA-A075-BCE1EEEBA45C.
70. Schmitzer-Torbert N, Jackson J, Henze D, Harris K, Redish AD. Quantitative measures of cluster quality for use in extracellular recordings. *Neuroscience*. 2005;131(1):1-11. doi:10.1016/j.neuroscience.2004.09.066
71. English DF, McKenzie S, Evans T, Kim K, Yoon E, Buzsáki G. Pyramidal cell-interneuron circuit architecture and dynamics in hippocampal networks. *Neuron*. 2017;96(2):505-520. doi:10.1016/j.neuron.2017.09.033.Pyramidal
72. Aghajan ZM, Acharya L, Moore JJ, Cushman JD, Vuong C, Mehta MR. Impaired spatial selectivity and intact phase precession in two-dimensional virtual reality. *Nat Neurosci*. 2014;18(1):121-128. doi:10.1038/nn.3884
73. Reifenstein ET, Ebbesen XCL, Tang Q, Brecht M, Schreiber S, Kempter XR. Cell-Type Specific Phase Precession in Layer II of the Medial Entorhinal Cortex. *J Neurosci*. 2016;36(7):2283-2288. doi:10.1523/JNEUROSCI.2986-15.2016
74. Kempter R, Leibold C, Buzsáki G, Diba K, Schmidt R. Quantifying circular-linear associations: Hippocampal phase precession. *J Neurosci Methods*. 2012;207(1):113-124. doi:10.1016/j.jneumeth.2012.03.007
75. Reifenstein E, Stemmler M, Herz AVM, Kempter R, Schreiber S. Movement dependence and layer specificity of entorhinal phase precession in two-dimensional environments. *PLoS One*. 2014;9(6). doi:10.1371/journal.pone.0100638
76. Schmidt R, Diba K, Leibold C, Schmitz D, Kempter R. Single-trial phase precession in the hippocampus. *J Neurosci*. 2009;29(42):13232-13241. doi:10.1523/JNEUROSCI.2270-09.2009.Single-trial
77. Skaggs WE, Mcnaughton BL, Gothard KM. An Information-Theoretic Approach to Deciphering the Hippocampal Code. In: *In: Advances in Neural Information Processing Systems*. ; 1993:1030-1037. doi:10.1109/EUMC.2007.4405137
78. Muller RU, Kubie JL. The firing of hippocampal place cells predicts the future position of freely moving rats. *J Neurosci*. 1989;9(12):4101-4110. doi:10.1523/jneurosci.09-12-04101.1989

79. Beed P, de Filippo R, Holman C, Johenning FW, Leibold C, Caputi A, Monyer H, Schmitz D. Layer 3 Pyramidal Cells in the Medial Entorhinal Cortex Orchestrate Up-Down States and Entrain the Deep Layers Differentially. *Cell Rep*. 2020;33(10):108470. doi:10.1016/j.celrep.2020.108470
80. Gomez JL, Bonaventura J, Lesniak W, Matthews WB, Sysa-Shah P, Rodriguez LA, Ellis RJ, Richie CT, Harvey BK, Dannals RF, Pomper MG, Bonci A, Michaelides M. Chemogenetics revealed: DREADD occupancy and activation via converted clozapine. 2017;507(August):503-507.
81. Mizuseki K, Royer S, Diba K, Buzsáki G. Activity dynamics and behavioral correlates of CA3 and CA1 hippocampal pyramidal neurons. *Hippocampus*. 2012;22(8):1659-1680. doi:10.1002/hipo.22002
82. Yizhar O, Fenno LE, Davidson TJ, Mogri M, Deisseroth K. Optogenetics in Neural Systems. *Neuron*. 2011;71(1):9-34. doi:10.1016/j.neuron.2011.06.004
83. Owen SF, Liu MH, Kreitzer AC. Thermal constraints on in vivo optogenetic manipulations. *Nat Neurosci*. 2019;22(7):1061-1065. doi:10.1038/s41593-019-0422-3
84. Chauvette S, Crochet S, Volgushev M, Timofeev I. Properties of slow oscillation during slow-wave sleep and anesthesia in cats. *J Neurosci*. 2011;31(42):14998-15008. doi:10.1523/JNEUROSCI.2339-11.2011
85. Clement EA, Richard A, Thwaites M, Ailon J, Peters S, Dickson CT. Cyclic and sleep-like spontaneous alternations of brain state under urethane anaesthesia. *PLoS One*. 2008;3(4). doi:10.1371/journal.pone.0002004
86. Suzuki M, Larkum ME. General Anesthesia Decouples Cortical Pyramidal Neurons. *Cell*. 2020;180(4):666-676.e13. doi:10.1016/j.cell.2020.01.024
87. Torao-Angosto M, Manasanch A, Mattia M, Sanchez-Vives M V. Up and Down States During Slow Oscillations in Slow-Wave Sleep and Different Levels of Anesthesia. *Front Syst Neurosci*. 2021;15(February):1-9. doi:10.3389/fnsys.2021.609645
88. Dasilva M, Camassa A, Navarro-Guzman A, Pazienti A, Perez-Mendez- L, Zamora-Lopez G, Mattia M, Sanchez-Vives MV. Modulation of cortical slow oscillations and complexity across anesthesia levels. *Neuroimage*. 2021;224(August 2020):117415. doi:10.1016/j.neuroimage.2020.117415
89. Hara K, Harris RA. The Anesthetic Mechanism of Urethane: The Effects on Neurotransmitter-Gated Ion Channels. *Anesth Pharmacol*. 2002;94:313-318.
90. Mahler S V., Aston-Jones G. CNO Evil? Considerations for the Use of DREADDs in Behavioral Neuroscience. *Neuropsychopharmacology*. 2018;43(5):934-936.

doi:10.1038/npp.2017.299

91. López AJ, Kramár E, Matheos DP, While AO, Kwapis J, Vogel-Ciernia A, Sakata K, Espinoza M, Wood MA. Promoter-specific effects of DREADD modulation on hippocampal synaptic plasticity and memory formation. *J Neurosci*. 2016;36(12):3588-3599. doi:10.1523/JNEUROSCI.3682-15.2016
92. Magee JC. Dendritic mechanisms of phase precession in hippocampal CA1 pyramidal neurons. *J Neurophysiol*. 2001;86(1):528-532. doi:10.1152/jn.2001.86.1.528
93. Thurley K, Leibold C, Gundlfinger A, Schmitz D, Kempter R. Phase precession through synaptic facilitation. *Neural Comput*. 2008;20(5):1285-1324. doi:10.1162/neco.2008.07-06-292
94. Ebbesen CL, Reifenstein ET, Tang Q, Burgalossi A, Ray S, Schreiber S, Kempter R, Brecht M. Cell Type-Specific Differences in Spike Timing and Spike Shape in the Rat Parasubiculum and Superficial Medial Entorhinal Cortex. *Cell Rep*. 2016:1-11. doi:10.1016/j.celrep.2016.06.057
95. D'Albis T, Jaramillo J, Sprekeler H, Kempter R. Hierarchical Reinforcement Learning for Sequencing Behaviors. *Neural Comput*. 2015;27:1624-1672. doi:10.1162/NECO
96. Wang M, Foster DJ, Pfeiffer BE. Alternating sequences of future and past behavior encoded within hippocampal theta oscillations. *Science*. 2020;370(6513):247-250. doi:10.1126/science.abb4151
97. Roy DS, Kitamura T, Okuyama T, Ogawa SK, Sun C, Obata Y, Yoshiki A, Tonegawa S. Distinct Neural Circuits for the Formation and Retrieval of Episodic Memories. *Cell*. 2017;170(5):1000-1012.e19. doi:10.1016/j.cell.2017.07.013
98. Ohara S, Blankvoort S, Nair RR, Nigro MJ, Eirik S, Kentros C, Witter MP. Local projections of layer Vb-to-Va are more prominent in lateral than in medial entorhinal cortex. *eLife* 2021;10:e67262 doi: 10.7554/eLife.67262.
99. Kitamura T, Pignatelli M, Suh J, Kohara K, Yoshiki A, Abe K, Tonegawa S. Island cells control temporal association memory. *Science*. 2014;343(6173):896-901. doi:10.1126/science.1244634
100. Canto CB, Wouterlood FG, Witter MP. What does the anatomical organization of the entorhinal cortex tell us? *Neural Plast*. 2008;2008. doi:10.1155/2008/381243
101. Marks WD, Yamamoto N, Kitamura T. Complementary roles of differential medial entorhinal cortex inputs to the hippocampus for the formation and integration of temporal and contextual memory (Systems Neuroscience). *Eur J Neurosci*. 2020;(March):1-18. doi:10.1111/ejn.14737

102. Digby RJ, Bravo DS, Paulsen O, Magloire V. Distinct mechanisms of Up state maintenance in the medial entorhinal cortex and neocortex. *Neuropharmacology*. 2017;113:543-555. doi:10.1016/j.neuropharm.2016.11.009
103. Yoshida M, Fransén E, Hasselmo ME. mGluR-dependent persistent firing in entorhinal cortex layer III neurons. *Eur J Neurosci*. 2008;28(6):1116-1126. doi:10.1111/j.1460-9568.2008.06409.x
104. Kentros CG, Agnihotri NT, Streater S, Hawkins RD, Kandel ER. Increased attention to spatial context increases both place field stability and spatial memory. *Neuron*. 2004;42(2):283-295. doi:10.1016/S0896-6273(04)00192-8
105. Du F, Eid T, Lothman EW, Köhler C, Schwarcz R. Preferential neuronal loss in layer III of the medial entorhinal cortex in rat models of temporal lobe epilepsy. *J Neurosci*. 1995;15(10):6301-6313. doi:10.1523/jneurosci.15-10-06301.1995
106. Du F, Whetsell WO, Abou-Khalil B, Blumenkopf B, Lothman EW, Schwarcz R. Preferential neuronal loss in layer III of the entorhinal cortex in patients with temporal lobe epilepsy. *Epilepsy Res*. 1993;16(3):223-233. doi:10.1016/0920-1211(93)90083-J
107. Marshall L, Helgadóttir H, Mölle M, Born J. Boosting slow oscillations during sleep potentiates memory. *Nature*. 2006;444(7119):610-613. doi:10.1038/nature05278
108. Herweg NA, Kahana MJ. Spatial Representations in the Human Brain. *Front Hum Neurosci*. 2018;12(July):1-16. doi:10.3389/fnhum.2018.00297
109. Qasim SE, Fried I, Jacobs J. Phase precession in the human hippocampus and entorhinal cortex. *bioRxiv*. 2020. doi:10.1101/2020.09.06.285320
110. Fu H, Rodriguez GA, Herman M, Emrani S, Nahmani E, Barrett G, Figueroa HY, Goldberg E, Hussani SA, Duff KE. Tau Pathology Induces Excitatory Neuron Loss , Grid Cell Dysfunction , and Spatial Memory Deficits Reminiscent of Early Alzheimer ' s Disease Report Tau Pathology Induces Excitatory Neuron Loss , Grid Cell Dysfunction , and Spatial Memory Deficits Reminis. *Neuron*. 2017;93(3):533-540.e6. doi:10.1016/j.neuron.2016.12.023
111. Lenck-Santini PP, Holmes GL. Altered phase precession and compression of temporal sequences by place cells in epileptic rats. *J Neurosci*. 2008;28(19):5053-5062. doi:10.1523/JNEUROSCI.5024-07.2008
112. Vlček K, Laczó J. Neural correlates of spatial navigation changes in mild cognitive impairment and Alzheimer's disease. *Front Behav Neurosci*. 2014;8(March):89. doi:10.3389/fnbeh.2014.00089
113. Schröder TN, Haak K V, Jimenez NIZ, Beckmann CF, Doeller CF. Functional topography

of the human entorhinal cortex. *Elife*. 2015;4(JUNE):1-17. doi:10.7554/eLife.06738

114. Domínguez-Álvaro M, Montero-Crespo M, Blazquez-Llorca L, DeFelipe J, Alonso-Nanclares L. 3D Ultrastructural Study of Synapses in the Human Entorhinal Cortex. *bioRxivAS*. 2020. doi:10.1093/cercor/bhaa233

10. Statutory Declaration

“I, Constance Holman, by personally signing this document in lieu of an oath, hereby affirm that I prepared the submitted dissertation on the topic “The role of medial entorhinal cortex layer three pyramidal cells in slow oscillations and spatial coding” independently and without the support of third parties, and that I used no other sources and aids than those stated.

All parts which are based on the publications or presentations of other authors, either in letter or in spirit, are specified as such in accordance with the citing guidelines. The sections on methodology (in particular regarding practical work, laboratory regulations, statistical processing) and results (in particular regarding figures, charts and tables) are exclusively my responsibility.

Furthermore, I declare that I have correctly marked all of the data, the analyses, and the conclusions generated from data obtained in collaboration with other persons, and that I have correctly marked my own contribution and the contributions of other persons (cf. declaration of contribution). I have correctly marked all texts or parts of texts that were generated in collaboration with other persons.

My contributions to any publications to this dissertation correspond to those stated in the below joint declaration made together with the supervisor. All publications created within the scope of the dissertation comply with the guidelines of the ICMJE (International Committee of Medical Journal Editors; www.icmje.org) on authorship. In addition, I declare that I shall comply with the regulations of Charité – Universitätsmedizin Berlin on ensuring good scientific practice.

I declare that I have not yet submitted this dissertation in identical or similar form to another Faculty.

The significance of this statutory declaration and the consequences of a false statutory declaration under criminal law (Sections 156, 161 of the German Criminal Code) are known to me.”

Date Signature

11. Detailed Declaration of Contribution

(Mary) Constance Holman had the following share in the following publication:

Beed, P*., **de Filippo, R.*, Holman, C***, Johenning, F.W., Leibold, C., Caputi, A., Monyer, H., and Schmitz, D. Layer 3 Pyramidal Cells in the Medial Entorhinal Cortex Orchestrate Up-Down States and Entrain the Deep Layers Differentially. *Cell Reports*. 2020.

Planning and design of the experiments:

The experiments were designed by C. Holman, P. Beed, R. De Filippo and D. Schmitz.

Performance of the experiments:

All surgeries and injections for *in vivo* experiments.
Recordings of up down states *in vivo* (Figure 1a-d).
Recordings and silencing of up down states in Oxr1 x Ai40D mice (Figure 3h-k)
Recordings and silencing of up down states using a closed-loop system in WT, Oxr1 x Ai40D and Uchl1-Cre mice (Figure S4).
Slicing, histology and imaging of above experiments.

Analysis of the experiments:

Code and analysis of above experiments.
Statistical analysis together with P. Beed.

Writing and editing the publication:

The publication was written and edited by C. Holman, P. Beed, and R. De Filippo in collaboration with F. Johenning, C. Leibold, A. Caputi, H. Monyer and D. Schmitz.

Other data included in this thesis:

Experiments designed in collaboration with J. Tukker, E. Reifenstein, R. Kempter and D. Schmitz.
All surgeries and injections.
All data collection, code, histology, imaging and analysis related to **Thesis Figures 5 – 8.**

_____

Signature, date and stamp of first supervising university professor / lecturer

_____

Signature of doctoral candidate

12. Journal Summary List Extract

Journal Data Filtered By: **Selected JCR Year: 2016** Selected Editions: SCIE,SSCI

Selected Categories: **“CELL BIOLOGY”** Selected Category Scheme: WoS

Gesamtanzahl: 189 Journale

Rank	Full Journal Title	Total Cites	Journal Impact Factor	Eigenfactor Score
1	NATURE REVIEWS MOLECULAR CELL BIOLOGY	40,565	46.602	0.095760
2	CELL	217,952	30.410	0.594680
3	NATURE MEDICINE	70,491	29.886	0.178660
4	CANCER CELL	32,653	27.407	0.102930
5	Cell Stem Cell	21,524	23.394	0.092500
6	NATURE CELL BIOLOGY	38,128	20.060	0.103150
7	Cell Metabolism	25,575	18.164	0.099760
8	Science Translational Medicine	22,073	16.796	0.125780
9	CELL RESEARCH	11,885	15.606	0.038060
10	TRENDS IN CELL BIOLOGY	12,503	15.333	0.035160
11	Annual Review of Cell and Developmental Biology	9,131	14.917	0.020370
12	MOLECULAR CELL	57,961	14.714	0.184330
13	NATURE STRUCTURAL & MOLECULAR BIOLOGY	26,851	12.595	0.092870
14	TRENDS IN MOLECULAR MEDICINE	8,371	10.732	0.019460
15	CURRENT OPINION IN CELL BIOLOGY	13,266	9.937	0.029670

16	EMBO JOURNAL	66,603	9.792	0.097800
17	GENES & DEVELOPMENT	57,493	9.413	0.105240
18	DEVELOPMENTAL CELL	25,598	9.174	0.076190
19	CURRENT BIOLOGY	52,274	8.851	0.134880
20	Cold Spring Harbor Perspectives in Biology	11,216	8.769	0.056260
21	PLANT CELL	49,595	8.688	0.074660
22	Autophagy	12,494	8.593	0.032420
23	EMBO REPORTS	11,985	8.568	0.032790
24	Cell Systems	394	8.406	0.002250
25	CELL DEATH AND DIFFERENTIATION	17,711	8.339	0.034080
26	Cell Reports	20,705	8.282	0.158610

13. Copy of Paper

Report

Cell Reports

Layer 3 Pyramidal Cells in the Medial Entorhinal Cortex Orchestrate Up-Down States and Entrain the Deep Layers Differentially

Graphical Abstract

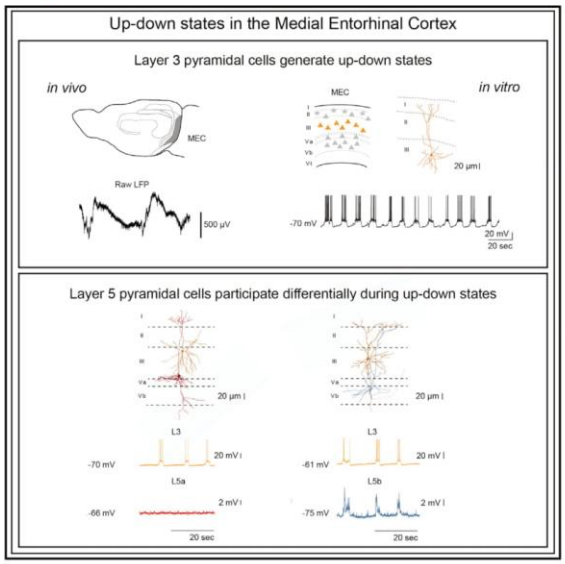

Authors

Prateep Beed, Roberto de Filippo, Constance Holman, ..., Antonio Caputi, Hannah Monyer, Dietmar Schmitz

Correspondence

prateep.beed@charite.de (P.B.), dietmar.schmitz@charite.de (D.S.)

In Brief

Beed et al. show that layer 3 of the medial entorhinal cortex is necessary and sufficient to generate up-down states locally. This activity propagates differentially to the deeper layers based on the synaptic connectivity between these layers. Layer 5b, which receives hippocampal output, is preferentially activated.

Highlights

- Layer 3 medial entorhinal cortex (L3 MEC) generates up-down states (UDS)
- Inactivation of L3 MEC suppresses UDS
- Two sublayers of L5 MEC differentially participate during UDS
- UDS propagate from L3 to L5b with high fidelity

Beed et al., 2020, Cell Reports 33, 108470
December 8, 2020 © 2020 The Author(s).
https://doi.org/10.1016/j.celrep.2020.108470

CellPress

Cell Reports

CellPress
OPEN ACCESS

Report

Layer 3 Pyramidal Cells in the Medial Entorhinal Cortex Orchestrate Up-Down States and Entrain the Deep Layers Differentially

Prateep Beed,[1,2,9,10,*] Roberto de Filippo,[1,9] Constance Holman,[1,9] Friedrich W. Johenning,[1,2,7] Christian Leibold,[3,4] Antonio Caputi,[5] Hannah Monyer,[5] and Dietmar Schmitz[1,2,6,7,8,*]

[1]Charité—Universitätsmedizin Berlin, Neuroscience Research Center, 10117 Berlin, Germany
[2]Berlin Institute of Health, 10178 Berlin, Germany
[3]Department Biologie II, Ludwig-Maximilians-Universität München, 82152 Munich, Germany
[4]Bernstein Center for Computational Neuroscience Munich, 82152 Munich, Germany
[5]Department of Clinical Neurobiology, Medical Faculty of Heidelberg University and German Cancer Research Center (DKFZ), Im Neuenheimer Feld 280, 69120 Heidelberg, Germany
[6]German Center for Neurodegenerative Diseases (DZNE) Berlin, 10117 Berlin, Germany
[7]Cluster of Excellence NeuroCure, 10117 Berlin, Germany
[8]Einstein Center for Neurosciences Berlin, 10117 Berlin, Germany
[9]These authors contributed equally
[10]Lead Contact
*Correspondence: prateep.beed@charite.de (P.B.), dietmar.schmitz@charite.de (D.S.)
https://doi.org/10.1016/j.celrep.2020.108470

SUMMARY

Up-down states (UDS) are synchronous cortical events of neuronal activity during non-REM sleep. The medial entorhinal cortex (MEC) exhibits robust UDS during natural sleep and under anesthesia. However, little is known about the generation and propagation of UDS-related activity in the MEC. Here, we dissect the circuitry underlying UDS generation and propagation across layers in the MEC using both *in vivo* and *in vitro* approaches. We provide evidence that layer 3 (L3) MEC is crucial in the generation and maintenance of UDS in the MEC. Furthermore, we find that the two sublayers of the L5 MEC participate differentially during UDS. Our findings show that L5b, which receives hippocampal output, is strongly innervated by UDS activity originating in L3 MEC. Our data suggest that L5b acts as a coincidence detector during information transfer between the hippocampus and the cortex and thereby plays an important role in memory encoding and consolidation.

INTRODUCTION

During non-rapid eye movement (NREM) sleep, many cortical structures display synchronous activity that is characterized by slow-wave oscillatory activity (<1 Hz). Slow-wave oscillatory activity is characterized by alternating between active (depolarized) up states and quiescent (hyperpolarized) down states of neurons, which constitute a sequence of up-down states (UDS). UDS were reported to occur in many species and were detected in several cortical structures (Nir et al., 2011; Steriade et al., 1993; Wilson and Groves, 1981; for a review, see Tukker et al., 2020). It has been shown that UDS can entrain entire cortical columns and propagate between cortical areas as traveling waves (Massimini et al., 2004; Luczak et al., 2007; for a review, see Neske, 2016). The role of UDS is proposed to facilitate information transfer between memory-encoding structures such as the hippocampus and memory consolidation structures in the neocortex (for a review, see Neske, 2016) by influencing synaptic transmission (Bartram et al., 2017) and plasticity (González-Rueda et al., 2018). UDS have been observed during natural sleep (Vyazovskiy et al., 2011) under anesthesia (Steriade et al., 1993; Wilson and Groves, 1981) and in brain slices (Mann et al., 2009; Sanchez-Vives and McCormick, 2000; Tahvildari et al., 2012). The similarities in the spatiotemporal organization of UDS *in vivo* and *in vitro* enable studies of the underlying circuitry for the generation, propagation, and modulation of UDS at different resolutions by using different techniques.

The entorhinal cortices situated in the temporal lobe are known to be an important relay center for neuronal information between the hippocampus and neocortex. *In vivo* (Hahn et al., 2012; Isomura et al., 2006) and *in vitro* UDS have been described both in the lateral (Namiki et al., 2013) and medial (Mann et al., 2009; Tahvildari et al., 2012) parts of the entorhinal cortices. The medial entorhinal cortex (MEC) is involved in spatial information processing and memory. Recent studies in the MEC addressed questions pertaining to the stability of spatial maps (place and grid cells) during sleep (Gardner et al., 2019; Trettel et al., 2019). Therefore, a better understanding of the local circuit architecture that could maintain and propagate rhythmic activity during different sleep cycles and especially during UDS is gaining importance.

Previous studies provided evidence that UDS activity can be recorded *in vitro* in slice preparations of the MEC. Local field potential and single-cell recordings in superficial layers of the MEC revealed robust slow oscillatory activity indicative of UDS (Mann et al., 2009; Salkoff et al., 2015; Tahvildari et al., 2012). Excitatory and inhibitory neurons in layer 2 (L2) and L3 of the MEC were shown to be active during UDS (Neske et al., 2015; Tahvildari et al., 2012), and inhibition was demonstrated to play an important role in the termination of up states (Craig et al., 2013; Mann et al., 2009).

Although the circuitry that underlies UDS in the MEC has been investigated, questions regarding the generation and propagation of this activity across the laminar architecture of MEC (especially in the deeper layers) remain unanswered. Using *in vivo* recordings, *in vitro* population imaging of calcium activity, and *in vitro* multi-patch recordings, we show in this study that the generation of UDS activity originates in L3 and propagates to L5 of the MEC. Interestingly, L5 pyramidal cells differentially participate during UDS in the MEC—in particular, L5b pyramidal cells, which also receive hippocampal output (Sürmeli et al., 2015), receive UDS-related input from L3 pyramidal cells, whereas L5a pyramidal cells are not recruited. This differential processing of cortical UDS in the deeper layers of the MEC could have wider implications for the circuitry underlying information transfer and memory consolidation between the hippocampus and the cortex (Kitamura et al., 2017; Ohara et al., 2018; Roy et al., 2017).

RESULTS

Up-Down States in the MEC

We recorded stable *in vivo* UDS in the MEC of anesthetized wild-type mice (C57Bl6/n under urethane anesthesia; Figures 1A–1C). Both the frequency (five recordings from five animals; median frequency in the first 5 min ± interquartile range [IQR] = 0.1500 ± 0.0117, average frequency = 0.1480 Hz; median frequency in the last 5 min ± IQR = 0.1500 ± 0.0558, average frequency = 0.1613 Hz; p = 0.8175, U = 11, Mann-Whitney U test) and up state duration (five recordings from five animals; median duration in first 5 min ± IQR = 1.855 ± 0.3187, average duration = 1.51 s, median duration in last 5 min ± IQR = 1.5338 ± 0.9538, average duration = 1.756 s; p = 0.4206, U = 8, Mann-Whitney U test) were stable across several minutes of recording (Figure 1D). These measurements are consistent with previously published reports on UDS in the MEC under urethane anesthesia (Isomura et al., 2006; Hahn et al., 2012). Silicon probes were positioned in the superficial layers of the MEC (recording sites mostly in L3; Figure 1B) and slow wave oscillations with nested gamma oscillations were recorded (Figure 1C). We proceeded with an *in vitro* model of UDS in the MEC to investigate in more detail the circuitry that can support the generation and propagation of such slow wave activity.

Since UDS is a population activity, we decided to use mice expressing the genetically encoded calcium indicator GCamp6f in pyramidal cells in the neocortex by breeding these mice with Nex-Cre mice (Goebbels et al., 2006). This enabled us to image UDS activity at the population level to test for synchronous activation of L3 pyramidal cells in our *in vitro* model (Figure S1). We imaged the superficial layers of the MEC in five slices from two animals and analyzed between 20 and 33 cells per slice. In sum, we detected 42 synchronous events with coactive cells in a time window of 1 s. In 50% of these events, we observed >10 coactive cells (median of active cells ± IQR: 11.5 ± 17; Figures S1A–S1D).

Up-Down States in L3 MEC

It has been shown previously that several cell types, including excitatory and inhibitory neurons in the superficial layers of the MEC, take part in UDS (L1–L3, Mann et al., 2009; Tahvildari et al., 2012). To further differentiate single-cell activity during UDS, we used a multi-patch approach and recorded such slow-wave oscillatory activity simultaneously from two to four cells in the superficial layers of the MEC (Figures 1E and 1F). Based on simultaneously recorded L3 and L2 excitatory cells (L3 = nine cells, L2 = 10 cells; Figures S2A and S2B), we determined that L3 pyramidal cells were the most active cell population. L3 MEC pyramidal cells exhibited a higher spike probability (L3 = 71.26% ± 11.67%, L2 = 18.41% ± 9.29%, p = 0.0029, Mann-Whitney U test) and number of spikes per up state (L3 = 5.26 ± 1.18, L2 = 1.24 ± 0.50, p = 0.0042, Mann-Whitney U test) compared to those in L2 stellate cells (Figure S2B). Thereafter we focused only on dorsal MEC L3 pyramidal cells and extended our analysis by recording from L3 duplets, triplets, or quadruplets. We quantified the up state duration (1.76 ± 0.14 s, n = 33 cells; Figure 1H, first panel) and frequency (0.087 ± 0.008 Hz, n = 33 cells; Figure 1H, second panel) from L3 pyramidal cells and found that our results were congruent with previously reported values (Mann et al., 2009; Tahvildari et al., 2012).

Local MEC Circuitry Can Sustain Up-Down State Activity

Next, we asked whether the MEC alone is endowed with the minimum circuitry necessary to generate and maintain UDS. To this end, we prepared mini-slices of the MEC by making incisions and removing the lateral entorhinal cortex (LEC), hippocampus, and the parahippocampal structures such as the pre- and parasubiculum. L3 pyramidal cells in the mini-slices of the MEC showed robust UDS activity reminiscent of that in intact slices. Up state duration (2.96 ± 0.12 s, n = seven cells; Figure 1H, third panel) was longer in mini-slices (p = 0.0002, Mann-Whitney U test), and up state frequency (0.109 ± 0.015Hz, n = seven cells; Figure 1H, fourth panel) was comparable between mini-slices and intact slices (p = 0.147, Mann-Whitney U test). Hence, we conclude that the isolated MEC, and particularly L3, comprises the circuitry that generates and maintains UDS.

Up-Down States Are Largely Suppressed in the MEC by Silencing L3

Knowing that L3 MEC is the most active layer during UDS, we sought to silence the activity of L3 pyramidal cells to study the impact on UDS in the MEC. We reasoned that silencing L3 pyramidal cells would abolish field UDS activity, if L3 were the generating layer. Alternatively, if other layers in the MEC were responsible and activity propagated to L3, then we would still be able to detect field UDS activity. As a first approach, we uncaged GABA locally on L3 in the MEC during ongoing UDS activity (Figures 2A and 2B). We used a closed-loop photostimulation approach in

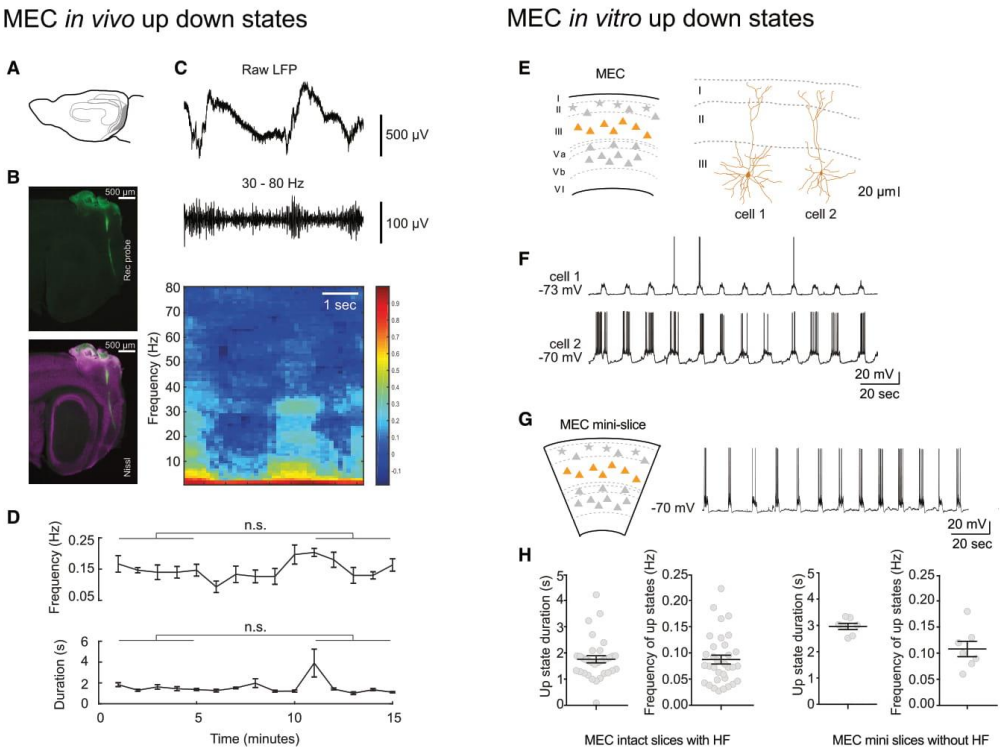

Figure 1. Up-Down States (UDS) in the MEC

(A) Schematic of the sagittal view of the mouse brain, where the MEC is shaded in gray.

(B) Example *in vivo* recordings under urethane anesthesia were targeted to L3 of MEC, as shown by the silicon probe location (top panel in green) and overlay with NeuN staining (lower panel in purple) sagittal section.

(C) UDS from L3 MEC showing slow oscillations (upper panel) with nested gamma frequency oscillations (center panel, band-pass filtered from 30 to 80 Hz). Lower panel shows the spectrogram of the trace above calculated using a Stockwell transform.

(D) Up state frequency and duration remains stable over time under urethane-anesthetized recording conditions (n = five recordings from five animals).

(E) *In vitro* model for UDS in the MEC. L3 is marked in orange. The right panel shows two L3 MEC cells with dense basal dendrites and apical dendrites reaching to the pial surface.

(F) Raw traces showing alternating UDS from the two cells shown in (E) above.

(G) Mini-slices of the MEC were prepared by removing the adjoining hippocampal structures and the presubiculum, parasubiculum, and LEC. The right panel shows a recording from a L3 MEC pyramidal cell demonstrating robust UDS in a reduced mini-slice of the MEC.

(H) Left panel: up state duration and frequency (n = 33 cells) in intact slices with hippocampal formation (HF); right panel: in a mini-slice of the MEC (n = seven cells) without HF.

Data are presented as means ± SEMs. n.s. (non significant) for $p > 0.05$, *$p < 0.05$ and **$p < 0.01$.

which, as soon as a spike on an up state was detected, blue light was triggered for 500 ms to uncage Rubi-GABA locally. Upon uncaging, we detected an immediate hyperpolarization of the membrane potential to a down state, thereby significantly shortening the up state duration (no uncaging average duration: 3.09 ± 0.07 s, L3 uncaging average duration: 1.79 ± 0.15 s, $p < 0.0001$, Mann-Whitney *U* test; Figure 2C). Subthreshold events where no spikes were detected were not suppressed, and the average duration of these subthreshold up states during photostimulation trials was not significantly different from baseline (no uncaging) trials (no uncaging average duration: 2.43 ± 0.21 s, L3 uncaging average duration: 2.63 ± 0.10 s, $p = 0.1427$, Mann-Whitney *U* test; Figure 2D). The frequency of up states remained unaltered during L3 uncaging and no uncaging trials (no uncaging average frequency: 0.072 ± 0.008Hz, L3 uncaging average frequency: 0.069 ± 0.018Hz, $p = 0.9365$, Mann-Whitney *U* test; Figure 2E). We also analyzed the shortening of up states by defining the duration as the time between the 1st spike on an up state to the termination of that particular up state. The duration was significantly different between L3 uncaging and no

Up state triggered suppression of up states in L3 *(in vitro)*

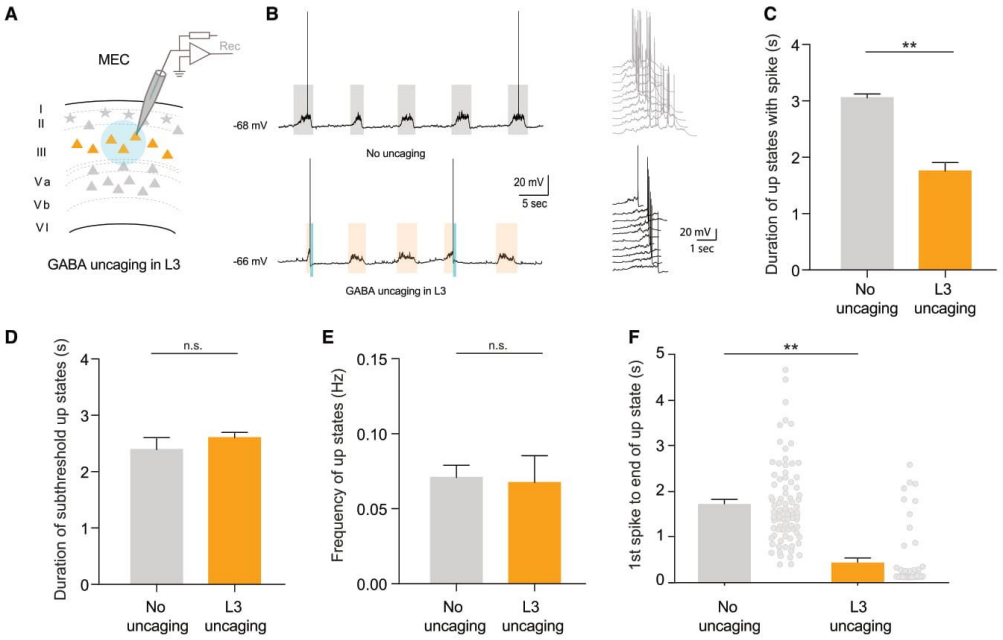

Figure 2. *In Vitro* Spontaneous Up States in the MEC Can Be Suppressed by L3 Hyperpolarization

(A) Schematic of closed-loop GABA uncaging experiments for spontaneously occurring up states. As soon as an up state with spikes was detected, 500 ms of caged GABA was uncaged using blue LED (488 nm) in L3 with no uncaging as control.

(B) Example traces of control (no uncaging) versus GABA uncaging in L3 following a spike on the up state. The shaded gray and orange represent the width of the detected up states. The right panel shows cutout up states in control (above, gray) versus GABA uncaging in L3 (below, black).

(C) Duration of up states with spikes were reduced when GABA was uncaged in L3 compared (n = 41 up states from five cells) to no uncaging control (n = 84 up states from five cells).

(D) Duration of up states without spikes, which occurred intermittently to those with spikes, was unaltered between the two conditions (no uncaging: n = 23 up states from five cells; L3 uncaging: n = 62 up states from five cells).

(E) Frequency of up states was unaltered (n = five cells for each condition).

(F) The time from the 1st to the end of up state as a measure of up state silencing shows that GABA uncaging in L3 (n = 41 up states from five cells) effectively shortened and suppressed the up state as compared to the no uncaging controls (n = 84 up states from five cells).

Data are presented as means ± SEMs. n.s. (non significant) for $p > 0.05$, *$p < 0.05$ and **$p < 0.01$.

uncaging trials, suggesting that GABA uncaging locally on L3 in the MEC immediately triggered a down state (no uncaging average duration: 1.73 ± 0.10 s, L3 uncaging average duration: 0.43 ± 0.11 s, $p < 0.0001$, Mann-Whitney *U* test; Figure 2F). Furthermore, hyperpolarizing the deeper layers, namely L5, had no suppressive effect on UDS activity in the MEC. Thus, both spontaneous (Figures S3A–S3C) and evoked (Figures S3D–S3F) up states remained unchanged.

Next, we crossed Oxr1-Cre mice (Suh et al., 2011) with an ArchT (Ai40D) line to express the inhibitory opsin selectively in L3 pyramidal cells in the MEC (Figure 3A1). We verified the spatial selectivity of the expression by co-staining for Wfs1, which marks L2 pyramidal cells (Kitamura et al., 2014). We found no co-expression of GFP (i.e., Oxr1^{+} putative L3 pyramidal cells) and Wfs1 (i.e., putative L2 pyramidal cells) (Figure 3A2). The GFP expression had a sharp border between L3 and L2, and it was possible to detect terminal branching of the L3 dendrites in L1. As expected, we also saw axonal terminals of L3 MEC pyramidal cells both in the proximal CA1 and distal subiculum, as reported by others for this mouse line (data not shown; Suh et al., 2011). Thereafter, we used *in vitro* slices to quantify the extent of light-induced hyperpolarization L3 pyramidal cells receive (Figures 3B–3E). In current clamp mode, cells were hyperpolarized on average by 3.46 ± 0.43 mV, n = 18 cells (Figure 3E) at resting membrane potential, and in voltage clamp (clamped at −60 mV), light-induced hyperpolarization was on average 20.18 ± 2.45 pA,

Oxr1-Cre x Ai40D (ArchT) characterization

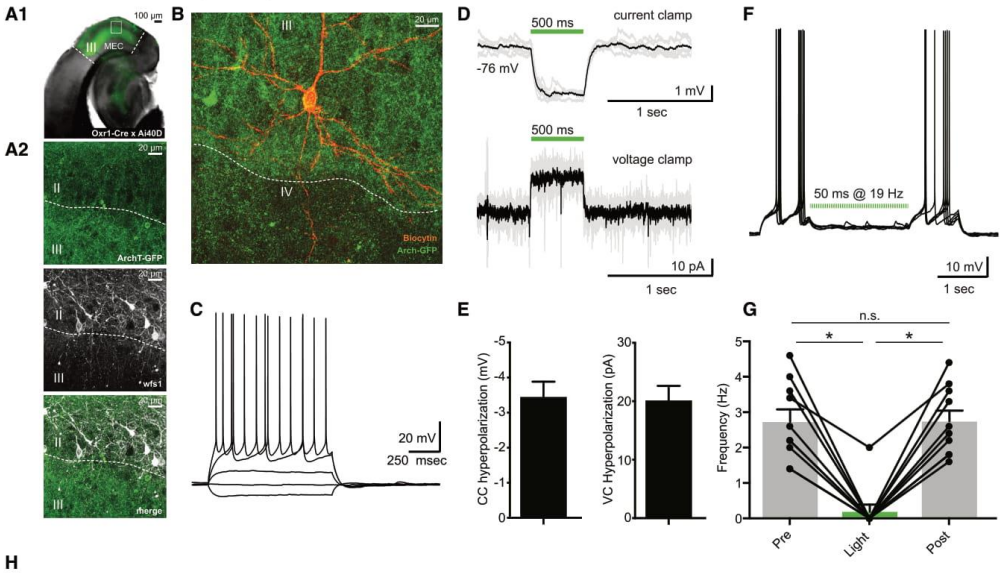

H

Reduction in in vivo incidence of UDS by silencing L3 MEC

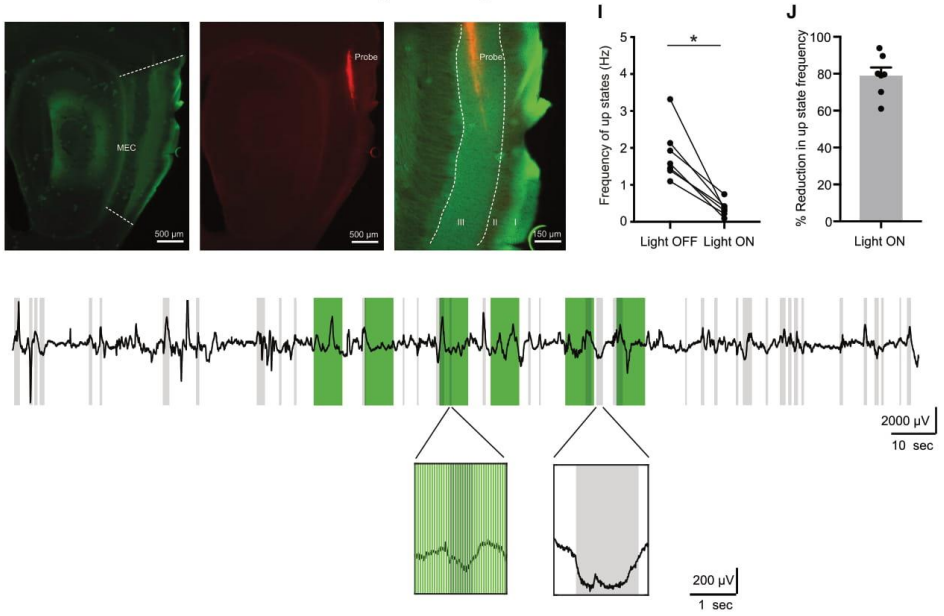

(legend on next page)

n = nine cells (Figure 3E). This prompted the question of whether this hyperpolarization sufficed to suppress spiking in L3 pyramidal cells. Thus, while we injected a 35-pA current for 4 s to evoke spikes, we shone light using a repetitive stimulus of 19 Hz and a pulse width of 50 ms for 2 s (Figure 3F). We were able to completely suppress spiking in 8/9 cells (Figure 3G). In the pre-light period, the frequency of spiking was on average 2.74 ± 0.35 Hz, during light stimulation there was a reduction to 0.2 ± 0.2 Hz, and a subsequent recovery to 2.75 ± 0.31 Hz in the post-light period (2-way ANOVA with multiple comparisons: $p < 0.0001$ for pre versus light, $p < 0.0001$ for light versus post, and $p = 0.99$ for pre versus post).

Inhibition of L3 Pyramidal Cells Suppresses the Frequency of Up States *In Vivo*

Next, we recorded UDS *in vivo* in anesthetized animals as described earlier (Figures 1A–1C) using silicon optrodes. We established a stable baseline of UDS in L3 MEC in Oxr1-Cre x Ai40D mice and then used green light light-emitting diode (LED) (525 nm) to activate archaerhodopsin and silence Oxr1$^+$ L3 pyramidal cells directly at the recording site (Figure 3H). The green bars show light ON periods in Figure 3K, and the detected up states are marked with gray-shaded areas. Silencing L3 pyramidal cells caused a large reduction in UDS activity during light ON periods compared to matched light OFF periods (Figures 3I and 3J). During light OFF periods, up states occurred with a median frequency ± IQR of 1.5791 ± 0.6752 Hz, average = 1.84 Hz. During light ON periods, up states were detected with a median frequency ± IQR of only 0.3402 ± 0.1780 Hz, average = 0.209 Hz, or an average reduction of 79.1% ($p = 0.016$, $Z = -2.3664$, n = seven recordings from seven animals, Wilcoxon signed rank test). We conclude that L3 MEC pyramidal cells are crucial in generating UDS in the MEC.

Our results using optogenetic inhibition suggest that L3 pyramidal cells are crucial for the generation of UDS in the MEC. However, we wondered whether L3 activity could be controlled in a more time-locked fashion during ongoing UDS activity *in vivo*. Therefore, we used a closed-loop stimulation system that guaranteed the firing of a light pulse each time an up state was detected in anaesthetized mice (see Method Details; Figures S4A–S4C). Here, we found that closed-loop stimulation of L3 pyramidal cells in Oxr1-Cre x Ai40D induced only a subtle, non-significant reduction of up state frequency (median baseline frequency ± IQR = 0.27 ± 0.2458 Hz, average baseline frequency = 0.2693 Hz, median stimulation frequency = 0.14 ± 0.1908 Hz, average stimulation frequency = 0.1700 Hz; $p = 0.1250$, $Z = -1.7529$ Wilcoxon signed rank test, five recordings from five animals; Figure S4D), and the duration of up states was unchanged (median baseline duration ± IQR = 1.13 ± 1.5701 s, average baseline duration = 1.8784 s, median stimulation duration = 1.32 ± 1.5644 s, average stimulation duration = 2.0101 s, $p = 0.0625$, $Z = -2.0226$, Wilcoxon signed rank test, five recordings from five animals; Figure S4E).

As a control, we repeated the experiment using wild-type mice that were not injected with an optogenetic construct (data not shown). Here, up state-triggered LED activation in L3 led to a trend of increasing upstate frequency (median baseline frequency ± IQR = 0.14 ± 0.0671 Hz, average baseline frequency = 0.1367 Hz, median stimulation frequency = 0.22 ± 0.1750 Hz, average stimulation frequency = 0.1807 Hz, $p = 0.1875$, $Z = -1.4832$, Wilcoxon signed rank test, five recordings from four animals), while also not interfering with their duration (median baseline duration ± IQR = 1.46 ± 0.5085 s, average baseline duration = 1.4278 s, median stimulation duration = 1.49 ± 0.5339 s, average stimulation duration = 1.4852 s, $p = 0.3125$, $Z = -1.2136$, Wilcoxon signed rank test, five recordings from four animals; data not shown).

Our *in vitro* experiments indicated that L2 cells were much less active than L3 cells during up states (Figure S2). L2 stellate cells receive strong feedforward projections from L3 pyramidal cells (Winterer et al., 2017), and they selectively target L5b pyramidal cells (Sürmeli et al., 2015). Thus, we took recourse to the Uchl1 mouse line, which allows specific targeting of L2 stellate cells in the MEC (Fuchs et al., 2016), to test whether manipulating L2 neuronal activity interferes with up state dynamics *in vivo*. Using the same optogenetic protocol on Uchl1-Cre mice injected with adeno-associated virus (AAV) conditionally transducing halorhodopsin (Uchl1-Cre x AAV-eNpHR3.0-EGFP; Figures S4F and S4G), we found that, akin to wild-type controls, optogenetic activation of L2 led to a very slight increase in up state frequency (median baseline frequency ± IQR = 0.25 ± 0.2185 Hz, average = 0.2788 Hz, median stimulation frequency = 0.31 ± 0.1733 Hz, average = 0.3250 Hz, $p = 0.1250$, $Z = -1.8257$, Wilcoxon signed rank test, four recordings from three animals; Figure S4H) and no

Figure 3. L3-Specific Optogenetic Inactivation Suppresses *In Vivo* UDS in MEC

(A1) Oxr1-Cre x Ai40D showing specific expression of ArchT in L3 MEC pyramidal cells. The rectangular box is magnified in A2.

(A2) GFP expression is specifically restricted to L3 (top panel, Wfs1 staining delineates the border to L2 (center panel). The merge shows the specificity of the Oxr1 line to L3 MEC pyramidal cells.

(B and C) Biocytin filled L3 pyramidal cell in (B) and characterization of firing pattern in (C).

(D) Light-induced hyperpolarization in current and voltage clamp on single L3 pyramidal cells upon activation of ArchT using 550 nm light.

(E) Quantification of average light-induced hyperpolarization in current clamp (CC hyperpolarization, n = 18 cells) and voltage clamp (VC hyperpolarization, n = nine cells) on L3 pyramidal cells upon activation of ArchT using 550 nm light.

(F) Current injection-evoked spikes could be robustly suppressed by activating ArchT on individual L3 pyramidal cells.

(G) Reduction of spiking activity in L3 pyramidal cells upon ArchT activation (n = nine cells).

(H) Example sagittal section from L3 recording in MEC, showing GFP (left), DiI trace (center), and magnified overlay (right).

(I) Frequency of up states during light OFF periods compared to light ON epochs (n = seven recordings from seven animals).

(J) Percentage reduction in upstate frequency from values shown in (I).

(K) Above: example raw LFP trace from L3 optrode recording. Green-shaded areas indicate light stimulation (light ON periods), and gray-shaded areas show the detected up states. Below: segments of trace magnified to show up states during light ON and light OFF periods.

Data are presented as means ± SEMs. n.s. (non significant) for $p > 0.05$, *$p < 0.05$ and **$p < 0.01$.

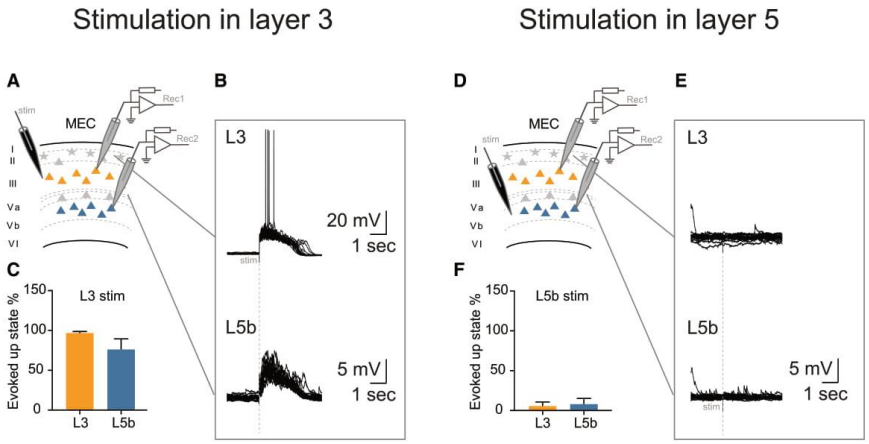

Figure 4. Up States Propagate Unidirectionally from L3 to Deeper Layers

(A) Schematic of the experimental setup. We evoked up states by stimulating in L3 (stim) and recording simultaneously from a L3 (Rec1) and a L5b (Rec2) pyramidal cell.

(B) Parallel recordings from L3 and L5b pyramidal cells while stimulating in L3 evokes reliable up states in both layers.

(C) High probability of evoking up states in L3 and L5b pyramidal cells by stimulating in L3 (n = nine cell pairs each having one L3 and one L5b pyramidal cell).

(D) Stimulation electrode was moved to L5b (stim) while recording from the same duplet (Rec1 and Rec2), as in (A).

(E) Parallel recordings from L3 and L5b pyramidal cells while stimulating in L5b failed to evoke reliable up states in either of the cells (n = nine cell pairs each having one L3 and one L5b pyramidal cell).

(F) Low probability of evoking up states in L3 and L5b pyramidal cells by stimulating in L5b.

Data are presented as means ± SEMs. n.s. (non significant) for $p > 0.05$, *$p < 0.05$ and **$p < 0.01$.

change in up state duration (median baseline duration ± IQR = 1.61 ± 0.9190 s, average = 1.5587 s, median stimulation duration = 1.52 ± 0.6700 s, average = 1.4271, $p = 0.1441$, $Z = 1.4606$, Wilcoxon signed rank test, four recordings from three animals; Figure S4I).

Taking these data together, a Kruskal-Wallis test demonstrated a near-significant difference in up state frequency across these three mouse lines ($H = 5.643$, $p = 0.0502$; Figure S4J). A Dunn's multiple comparisons test revealed that closed-loop stimulation produced a significant difference in frequency for Oxr1-Cre x Ai40D compared to wild-type mice ($p = 0.0467$), while there was no difference between wild-type and Uchl1-Cre x AAV-eNpHR3.0-EGFP mice ($p > 0.99$).

Up-Down States Propagate to Deeper Layers Unidirectionally

The deep layers of the MEC include two sublayers of L5 (L5a and L5b) and L6. Recently, L5 MEC has gained renewed attention in regard to pathways and cell types linked to memory consolidation (Ohara et al., 2018; Roy et al., 2017; Sürmeli et al., 2015). We wanted to better understand the propagation of entorhinal inputs during UDS from superficial to deeper layers, particularly in L5b, which also receives hippocampal output. To have a better temporal handle on UDS activity, we evoked up states via a stimulation electrode placed in L3 (evoked up states; Figures 4A and 4B; Mann et al., 2009). We saw robust and reproducible evoked up states in L3 pyramidal cells (9/9 cells). Simultaneously, we recorded L5b pyramidal cells, and we detected evoked up states in both L3 and L5b pyramidal cells (8/9 cells exhibited up states) upon stimulation in L3. The probabilities with which up states could be evoked were L3 97.78% ± 0.88% and L5b 77.22% ± 12.19% (Figure 4C). However, when we moved the stimulation electrode to L5b, we failed to evoke up states with reliable probability in either L5b or L3 pyramidal cells from the same cell pairs (Figures 4D and 4E). We did observe subthreshold depolarization, which could be classified as a putative up state, in 3/9 L5b pyramidal cells; however, the probability was <10% on average (L5b – 8.89% ± 6.16% and L3 – 6.67% ± 3.99%; Figure 4F). These results suggest that stimulation-evoked up states in L3 very likely propagate to deeper layers such as L5b. In contrast, up states could not be evoked by stimulating L5b circuits. Our data strongly suggest that L3 harbors the circuitry supporting the generation of up states and that these propagate unidirectionally to deeper layers.

L5b but Not L5a Pyramidal Cells Participate during Up-Down States in the MEC

L5 MEC can be subdivided into two sublayers, 5a (L5a) and 5b (L5b). L5a comprises etv1$^+$ excitatory cells and projects mostly to the cortex (Kitamura et al., 2017), whereas L5b contains ctip2$^+$ cells and receives input from the hippocampus (Sürmeli et al., 2015). To compare up state propagation between these two sublayers, we recorded either a L5a or a L5b pyramidal cell simultaneously with a L3 pyramidal cell during spontaneous

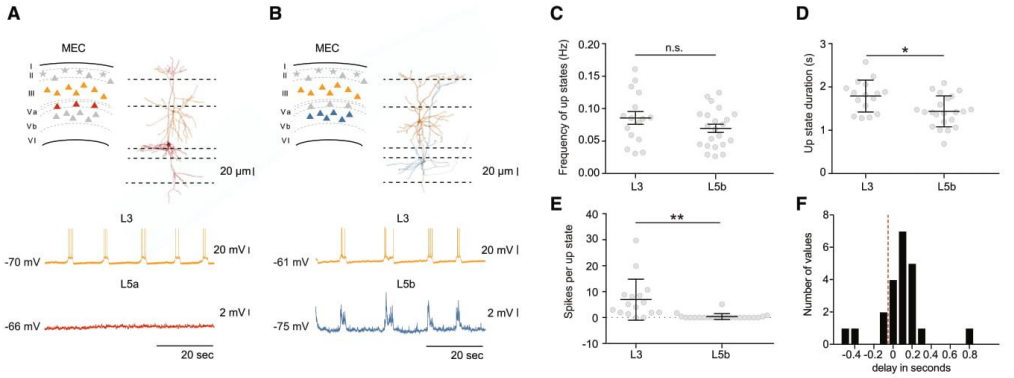

Figure 5. Differential Participation of L5 Pyramidal Cells during UDS

(A) Schematic of the experimental setup. Right panel: reconstruction of biocytin-filled cells with L3 pyramidal cell in orange and L5a pyramidal cell in red. Lower panel: upper trace from L3 pyramidal cell shows clear UDS, and lower trace from L5a pyramidal cell shows the absence of UDS activity.

(B) Schematic of the experimental setup. Right panel: reconstruction of biocytin-filled cells with L3 pyramidal cell in orange and L5b pyramidal cell in blue. Lower panel: upper trace from L3 pyramidal cell shows clear UDS, and lower trace from L5b cells shows synchronous UDS activity.

(C) Frequency of up states were not significantly different between L3 pyramidal cell (n = 16 cells) and L5b pyramidal cell (n = 22 cells). Most of the L5b pyramidal cells show synchronous UDS with L3 pyramidal cells, as shown in the trace in Figure 4B.

(D) Up state duration was shorter in L5b pyramidal cells (n = 22 cells) compared to L3 pyramidal cells (n = 16 cells).

(E) L5b pyramidal cells (n = 22 cells) mostly showed subthreshold depolarizations during up states with little or no spiking activity, unlike L3 pyramidal cells (n = 16 cells).

(F) L5b pyramidal cells followed L3 pyramidal cells as the onset of up states in L5b pyramidal cells experienced a delay when compared to L3 pyramidal cells. Data are presented as means ± SEMs. n.s. (non significant) for $p > 0.05$, *$p < 0.05$ and **$p < 0.01$.

UDS (Figures 5A and 5B). To our surprise, of all the duplet recordings from L3 and L5a pyramidal cells, none of the L5a pyramidal cells showed UDS activity, whereas all L5b pyramidal cells had UDS activity that was synchronous with L3 pyramidal cells (Figures 5A and 5B, lower panels). The frequency of up states was the same in the paired L3 and L5b recordings (L3 = 0.0858 ± 0.009 Hz, n = 16 cells; L5b = 0.0714 ± 0.006Hz, n = 22 cells; p = 0.2875, Mann-Whitney *U* test; Figure 5C), the duration of up states was shorter in L5b pyramidal cells compared to that of their paired L3 pyramidal cells (L3 = 1.79 ± 0.09 s, n = 16 cells; L5b = 1.44 ± 0.08 s, n = 22 cells; p = 0.016, Mann-Whitney *U* test; Figure 5D). Furthermore, unlike L3 pyramidal cells, L5b pyramidal cells hardly spiked on up states at resting membrane potential (L3 = 6.92 ± 1.98, n = 16 cells; L5b = 0.39 ± 0.24, n = 22 cells; $p < 0.0001$, Mann-Whitney *U* test; Figure 5E). We analyzed the temporal relationship between L3 and L5b pyramidal cells and found that most pyramidal cells in L5b followed the paired L3 pyramidal cell (with a delay of ~100 ms; Figure 5F), thereby confirming that in MEC, UDS activity propagates from L3 to L5b.

To conclude, we asked whether the absence of up state propagation to L5a pyramidal cells was due to a lack of synaptic connectivity between L3 and L5a pyramidal cells. We mapped L3 pyramidal cell inputs onto both L5a and L5b pyramidal cells using the Oxr1 x Chr mice and observed that L5a receive no monosynaptic inputs from L3 pyramidal cells (Figure S5). On the contrary, L5b pyramidal cells received strong and monosynaptic inputs from L3 pyramidal cells, thereby showing synchronized activity during UDS with L3 pyramidal cells.

DISCUSSION

During NREM sleep, the cortex enters a synchronous state characterized by rhythmic UDS. As was previously shown both *in vivo* (Hahn et al., 2012; Isomura et al., 2006) and *in vitro* (Mann et al., 2009; Tahvildari et al., 2012), we demonstrate here that the MEC exhibits prominent UDS activity. Since the MEC is laminated in distinct layers that are associated with different input-output projections, connectivity patterns, and cell types, a laminar profile of UDS activity could shed light on the generation and propagation of such activity. Our results indicate that L3 MEC is the site of origin for UDS in the MEC and that they propagate from there unidirectionally to deeper layers.

Previous work on UDS in the MEC focused on the participation of different neurons in the superficial layers, including excitatory (L3 and L2 cells) and inhibitory neurons (mainly L3; Tahvildari et al., 2012). It was shown that L3 pyramidal cells are most excitable compared to other cells types, and that parvalbumin interneurons are the most strongly modulated among the inhibitory neuron population during UDS in the MEC (Salkoff et al., 2015). It has also been shown that GABAergic transmission is important for the frequency of spikes during up states and in regulating the duration of up states (Mann et al., 2009). We extend these findings by using multi-patch recordings combined with optogenetics in a mouse line (Oxr1-Cre) that allows target specificity for L3 MEC, and show that L3 pyramidal cells in the MEC are the generators of UDS in the MEC. We analyzed and compared the spiking activity of L3 pyramidal cells to that of L2 and L5

excitatory neurons at the single-cell level and found that L3 had the most active cell population during UDS in the MEC. In addition, mini-slices of MEC exhibited UDS activity, thereby confirming that MEC alone contains the circuitry that is necessary to generate this slow-wave oscillatory activity.

The L3 MEC occupies an important position both structurally and functionally when considering cortico-hippocampal interactions. Our lab has previously shown that L3 is strongly connected to L2 stellate cells (Winterer et al., 2017). The findings of this study, and the availability of the L3 MEC-specific Cre mouse line, could prompt further investigation, addressing questions as to the role of L3 pyramidal cells during sleep, spatial memory, and behavior. The role of L3 pyramidal cells in development could also be explored. Of note, Namiki and colleagues (2013) studied L3 pyramidal cells in the lateral entorhinal cortex and detected synchronized waves between postnatal days 1 and 6. However, this activity may represent early network oscillations and may thus be different from UDS-related synchrony.

Our findings show that the two L5 sublayers (L5a and L5b) participate differentially during ongoing UDS activity. L5a sends output to distant cortical areas, including the prefrontal cortex (Kitamura et al., 2017; Sürmeli et al., 2015), nucleus accumbens, and amygdala, whereas L5b receives input from the hippocampus as well as from stellate cells in the MEC (Roy et al., 2017; Sürmeli et al., 2015). We report that L5a pyramidal cells do not participate in UDS activity in the MEC and receive no input from L3 pyramidal cells, whereas the activity of L5b is strongly synchronized and follows that of L3 pyramidal cells. This difference could be due to direct synaptic connections between L3 and L5b cells and a lack thereof between L3 and L5a cells (Figure S5). L5b has been shown to receive hippocampal output from both the subiculum and CA1 areas (Ohara et al., 2018), and therefore could be important for the cortical consolidation of hippocampal information by acting as a coincidence detector. As UDS occur *in vivo* during slow-wave NREM sleep, L5b forms an important structural and functional interface between hippocampal sharp wave activity and cortical UDS activity.

In conclusion, our finding that L3 orchestrates UDS within the MEC is an important piece of the puzzle for understanding entorhinal-hippocampal information flow. Up-down state transitions in superficial layers have been shown to propagate to the hippocampus (Sirota et al., 2003) and facilitate hippocampal sharp waves (Sirota et al., 2003; Isomura et al., 2006; Mölle et al., 2006). Conversely, sharp waves in CA1 precede sharp wave-like LFP patterns in the deep layers of the entorhinal cortex (Chrobak and Buzsáki, 1996). Thus, the local spread of UDS from L3 to L5b reported here may activate the hippocampus to replay stored patterns and at the same time set the L5b pyramidal cells in a "receive mode" to read out the hippocampal output in the form of integration or coincidence detection. Considering the findings presented here, one can envisage future studies to further dissect the role of different cortico-hippocampal pathways during slow-wave sleep and behavior.

STAR★METHODS

Detailed methods are provided in the online version of this paper and include the following:

SUPPLEMENTAL INFORMATION

Supplemental Information can be found online at https://doi.org/10.1016/j.celrep.2020.108470.

ACKNOWLEDGMENTS

We would like to thank Susanne Rieckmann and Anke Schönherr for excellent technical assistance. This work was supported by the Stiftung Charité, to P.B., H.M., and A.C.; the NeuroCure Cluster of Excellence; the DZNE; the Einstein Foundation; and the Deutsche Forschungsgemeinschaft (to D.S. [DFG Project number 327654276—SFB 1315, SFB 958, and Exc 257] and F.W.J. [JO1079/1-1; JO1079/3-1; and SFB665]).

AUTHOR CONTRIBUTIONS

P.B., C.H., F.W.J., A.C., H.M., and D.S. designed the experiments; P.B., R.d.F., C.H., and A.C. performed the research; P.B., R.d.F., C.H., F.W.J., and C.L. analyzed the data; P.B. wrote the paper with the help of R.d.F., C.H., F.W.J., A.C., H.M., and D.S. All of the authors read and edited the final version of the manuscript.

DECLARATION OF INTERESTS

The authors declare no competing interests.

Received: June 20, 2018
Revised: June 26, 2020
Accepted: November 10, 2020
Published: December 8, 2020

REFERENCES

Bartram, J., Kahn, M.C., Tuohy, S., Paulsen, O., Wilson, T., and Mann, E.O. (2017). Cortical up states induce the selective weakening of subthreshold synaptic inputs. Nat. Commun. *8*, 665.

Chrobak, J.J., and Buzsáki, G. (1996). High-frequency oscillations in the output networks of the hippocampal-entorhinal axis of the freely behaving rat. J. Neurosci. *16*, 3056–3066.

Craig, M.T., Mayne, E.W., Bettler, B., Paulsen, O., and McBain, C.J. (2013). Distinct roles of GABAB1a- and GABAB1b-containing GABAB receptors in spontaneous and evoked termination of persistent cortical activity. J. Physiol. *591*, 835–843.

Fuchs, E.C., Neitz, A., Pinna, R., Melzer, S., Caputi, A., and Monyer, H. (2016). Local and Distant Input Controlling Excitation in Layer II of the Medial Entorhinal Cortex. Neuron *89*, 194–208.

Gardner, R.J., Lu, L., Wernle, T., Moser, M.B., and Moser, E.I. (2019). Correlation structure of grid cells is preserved during sleep. Nat. Neurosci. *22*, 598–608.

Goebbels, S., Bormuth, I., Bode, U., Hermanson, O., Schwab, M.H., and Nave, K.A. (2006). Genetic targeting of principal neurons in neocortex and hippocampus of NEX-Cre mice. Genesis *44*, 611–621.

González-Rueda, A., Pedrosa, V., Feord, R.C., Clopath, C., and Paulsen, O. (2018). Activity-Dependent Downscaling of Subthreshold Synaptic Inputs during Slow-Wave-Sleep-like Activity In Vivo. Neuron *97*, 1244–1252.e5.

Hahn, T.T., McFarland, J.M., Berberich, S., Sakmann, B., and Mehta, M.R. (2012). Spontaneous persistent activity in entorhinal cortex modulates cortico-hippocampal interaction in vivo. Nat. Neurosci. *15*, 1531–1538.

Isomura, Y., Sirota, A., Ozen, S., Montgomery, S., Mizuseki, K., Henze, D.A., and Buzsáki, G. (2006). Integration and segregation of activity in entorhinal-hippocampal subregions by neocortical slow oscillations. Neuron *52*, 871–882.

Kitamura, T., Pignatelli, M., Suh, J., Kohara, K., Yoshiki, A., Abe, K., and Tonegawa, S. (2014). Island cells control temporal association memory. Science *343*, 896–901.

Kitamura, T., Ogawa, S.K., Roy, D.S., Okuyama, T., Morrissey, M.D., Smith, L.M., Redondo, R.L., and Tonegawa, S. (2017). Engrams and circuits crucial for systems consolidation of a memory. Science *356*, 73–78.

Luczak, A., Barthó, P., Marguet, S.L., Buzsáki, G., and Harris, K.D. (2007). Sequential structure of neocortical spontaneous activity in vivo. Proc. Natl. Acad. Sci. USA *104*, 347–352.

Madisen, L., Garner, A.R., Shimaoka, D., Chuong, A.S., Klapoetke, N.C., Li, L., van der Bourg, A., Niino, Y., Egolf, L., Monetti, C., et al. (2015). Transgenic mice for intersectional targeting of neural sensors and effectors with high specificity and performance. Neuron *85*, 942–958.

Mann, E.O., Kohl, M.M., and Paulsen, O. (2009). Distinct roles of GABA(A) and GABA(B) receptors in balancing and terminating persistent cortical activity. J. Neurosci. *29*, 7513–7518.

Massimini, M., Huber, R., Ferrarelli, F., Hill, S., and Tononi, G. (2004). The sleep slow oscillation as a traveling wave. J. Neurosci. *24*, 6862–6870.

Mölle, M., Yeshenko, O., Marshall, L., Sara, S.J., and Born, J. (2006). Hippocampal sharp wave-ripples linked to slow oscillations in rat slow-wave sleep. J. Neurophysiol. *96*, 62–70.

Namiki, S., Norimoto, H., Kobayashi, C., Nakatani, K., Matsuki, N., and Ikegaya, Y. (2013). Layer III neurons control synchronized waves in the immature cerebral cortex. J. Neurosci. *33*, 987–1001.

Neske, G.T. (2016). The Slow Oscillation in Cortical and Thalamic Networks: Mechanisms and Functions. Front. Neural Circuits *9*, 88.

Neske, G.T., Patrick, S.L., and Connors, B.W. (2015). Contributions of diverse excitatory and inhibitory neurons to recurrent network activity in cerebral cortex. J. Neurosci. *35*, 1089–1105.

Nir, Y., Staba, R.J., Andrillon, T., Vyazovskiy, V.V., Cirelli, C., Fried, I., and Tononi, G. (2011). Regional slow waves and spindles in human sleep. Neuron *70*, 153–169.

Ohara, S., Onodera, M., Simonsen, Ø.W., Yoshino, R., Hioki, H., Iijima, T., Tsutsui, K.I., and Witter, M.P. (2018). Intrinsic Projections of Layer Vb Neurons to Layers Va, III, and II in the Lateral and Medial Entorhinal Cortex of the Rat. Cell Rep. *24*, 107–116.

Pachitariu, M., Steinmetz, N., Kadir, S., Carandini, M., and Harris, K.D. (2016). Fast and accurate spike sorting of high-channel count probes with KiloSort. In Advances in Neural Information Processing Systems 29, D.D. Lee, M. Sugiyama, U.V. Luxburg, I. Guyon, and R. Garnett, eds.. https://discovery.ucl.ac.uk/id/eprint/1557035.

Roy, D.S., Kitamura, T., Okuyama, T., Ogawa, S.K., Sun, C., Obata, Y., Yoshiki, A., and Tonegawa, S. (2017). Distinct Neural Circuits for the Formation and Retrieval of Episodic Memories. Cell *170*, 1000–1012.e19.

Rueckl, M., Lenzi, S.C., Moreno-Velasquez, L., Parthier, D., Schmitz, D., Ruediger, S., and Johenning, F.W. (2017). SamuROI, a Python-Based Software Tool for Visualization and Analysis of Dynamic Time Series Imaging at Multiple Spatial Scales. Front. Neuroinform. *11*, 44.

Salkoff, D.B., Zagha, E., Yüzgeç, Ö., and McCormick, D.A. (2015). Synaptic Mechanisms of Tight Spike Synchrony at Gamma Frequency in Cerebral Cortex. J. Neurosci. *35*, 10236–10251.

Sanchez-Vives, M.V., and McCormick, D.A. (2000). Cellular and network mechanisms of rhythmic recurrent activity in neocortex. Nat. Neurosci. *3*, 1027–1034.

Schindelin, J., Arganda-Carreras, I., Frise, E., Kaynig, V., Longair, M., Pietzsch, T., Preibisch, S., Rueden, C., Saalfeld, S., Schmid, B., et al. (2012). Fiji: an open-source platform for biological-image analysis. Nat. Methods *9*, 676–682.

Schneider, C.A., Rasband, W.S., and Eliceiri, K.W. (2012). NIH Image to ImageJ: 25 years of image analysis. Nat. Methods *9*, 671–675.

Seamari, Y., Narváez, J.A., Vico, F.J., Lobo, D., and Sanchez-Vives, M.V. (2007). Robust off- and online separation of intracellularly recorded up and down cortical states. PLOS ONE *2*, e888.

Sirota, A., Csicsvari, J., Buhl, D., and Buzsáki, G. (2003). Communication between neocortex and hippocampus during sleep in rodents. Proc. Natl. Acad. Sci. USA *100*, 2065–2069.

Steriade, M., Nuñez, A., and Amzica, F. (1993). A novel slow (< 1 Hz) oscillation of neocortical neurons in vivo: depolarizing and hyperpolarizing components. J. Neurosci. *13*, 3252–3265.

Stockwell, R.G., Mansinha, L., and Lowe, R.P. (1996). Localization of the complex spectrum: the S transform. IEEE Trans. Signal Process. *44*, 998–1001.

Suh, J., Rivest, A.J., Nakashiba, T., Tominaga, T., and Tonegawa, S. (2011). Entorhinal cortex layer III input to the hippocampus is crucial for temporal association memory. Science *334*, 1415–1420.

Sürmeli, G., Marcu, D.C., McClure, C., Garden, D.L.F., Pastoll, H., and Nolan, M.F. (2015). Molecularly Defined Circuitry Reveals Input-Output Segregation in Deep Layers of the Medial Entorhinal Cortex. Neuron *88*, 1040–1053.

Tahvildari, B., Wölfel, M., Duque, A., and McCormick, D.A. (2012). Selective functional interactions between excitatory and inhibitory cortical neurons and differential contribution to persistent activity of the slow oscillation. J. Neurosci. *32*, 12165–12179.

Trettel, S.G., Trimper, J.B., Hwaun, E., Fiete, I.R., and Colgin, L.L. (2019). Grid cell co-activity patterns during sleep reflect spatial overlap of grid fields during active behaviors. Nat. Neurosci. *22*, 609–617.

Tukker, J.J., Beed, P., Schmitz, D., Larkum, M.E., and Sachdev, R.N.S. (2020). Up and Down States and Memory Consolidation Across Somatosensory, Entorhinal, and Hippocampal Cortices. Front. Syst. Neurosci. *14*, 22.

Vyazovskiy, V.V., Olcese, U., Hanlon, E.C., Nir, Y., Cirelli, C., and Tononi, G. (2011). Local sleep in awake rats. Nature *472*, 443–447.

Wilson, C.J., and Groves, P.M. (1981). Spontaneous firing patterns of identified spiny neurons in the rat neostriatum. Brain Res. *220*, 67–80.

Winterer, J., Maier, N., Wozny, C., Beed, P., Breustedt, J., Evangelista, R., Peng, Y., D'Albis, T., Kempter, R., and Schmitz, D. (2017). Excitatory Microcircuits within Superficial Layers of the Medial Entorhinal Cortex. Cell Rep. *19*, 1110–1116.

STAR★METHODS

KEY RESOURCES TABLE

REAGENT or RESOURCE	SOURCE	IDENTIFIER
Antibodies		
Streptavidin Alexa 488 Conjugate	Invitrogen	Cat# S32354; RRID: AB_2315383
Streptavidin Alexa 555 Conjugate	Invitrogen	Cat# s21381; RRID: AB_2307336
Rat monoclonal anti-CTIP2	Abcam	Cat# ab18465; RRID: AB_2064130
Rabbit monocloncal anti-WFS1	Proteintech	Cat# 11558-1-AP; RRID: AB_2216046
Chicken monocloncal anti-GFP	Abcam	Cat# ab92456; RRID: AB_10561923
Guinea pig monoclonal anti-NeuN	Merck	Cat# ABN90
Goat anti-rat Alexa 555 Conjugate	Invitrogen	Cat# A-21434; RRID: AB_141733
Goat anti-guinea pig Alexa 405 conjugate	Abcam	Abcam Cat# ab175678; RRID: AB_2827755
Bacterial and Virus Strains		
pAAV-Ef1a-DIO eNpHR 3.0-EYFP	Gift from Karl Deisseroth	Deisseroth stock
Chemicals, Peptides, and Recombinant Proteins		
Urethane	Sigma Aldrich	Cat #U2500
DiI	ThermoFisher	Cat #D3911
RuBi-GABA	Tocirs	Cat #3400
Deposited Data		
Raw and analyzed data	This paper	https://doi.org/10.6084/m9.figshare.13154321.v1 and upon author request
Experimental Models: Organisms/Strains		
Mouse:C57Bl6/n	Charité Forscchungseinrichtung für Experimentelle Medizin	N/A
Nex-Cre mice	Charité Forscchungseinrichtung für Experimentelle Medizin	RRID:MGI:3835559
Mouse: Ai95(RCL-GCaMP6f)-D	The Jackson Laboratory	JAX stock #024105
Mouse: C57BL/6N-Tg(Oxr1-cre)C14Stl/J	The Jackson Laboratory	JAX stock #030484
Mouse: Ai40(RCL-ArchT/EGFP)-D	The Jackson Laboratory	JAX stock #021188
Mouse: Ai32(RCL-ChR2(H134R)/EYFP)	The Jackson Laboratory	JAX stock # 012569
Mouse: STOCK Tg(Uchl1-cre)NO63Gsat/Mmucd	Mutant Mouse Resource and & Research Centers	RRID:MMRRC_036089-UCD
Software and Algorithms		
Fiji	Schindelin et al., 2012	https://fiji.sc/wiki/index.php/Fiji
ImageJ	Schneider et al., 2012	https://imagej.nih.gov/ij/
MATLAB 2019b	MathWorks	https://de.mathworks.com/?s_tid=gn_logo
Simulink	Mathworks	https://de.mathworks.com/products/simulink.html
Axon pClamp10 10.6.2	Molecular Devices	https://mdc.custhelp.com/app/answers/detail/a_id/18779/~/axon%E2%84%A2pclamp%E2%84%A2-10-electrophysiology-data-acquisition-%26-analysis-software-download
iQ live cell imaging software	Andor	https://andor.oxinst.com/products/iq-live-cell-imaging-software/
MAUDs Algorithm	Seamari et al., 2007	http://www.geb.uma.es/mauds
Kilosort2 (Pachitariu et al., 2016)	Pachitariu et al., 2016	https://github.com/MouseLand/Kilosort
Prism	GraphPad	https://www.graphpad.com/scientific-software/prism/
SAMUROI python package	Rueckl et al., 2017	https://github.com/samuroi/SamuROI
Code related to this paper	This paper	https://github.com/Schmitz-lab/MEC-Up-States and upon author request

(*Continued on next page*)

Continued

REAGENT or RESOURCE	SOURCE	IDENTIFIER
Other		
Neurostar Robot Stereotax	NeuroStar	https://robot-stereotaxic.com/drill-injection-robot/
Silicon probes and optrodes	NeuroNexus	https://neuronexus.com/wp-content/uploads/2018/11/2019_NNxCatalog_20181113.pdf
RHD2000 recording system	Intan	http://intantech.com/RHD_system.html
525nm PlexBright LED	Plexon	https://plexon.com/products/plexbright-table-top-modules/#1501022507108-0524a9b7-10bf
BNC-2110 Shielded Connector Block	National Instruments	Cat # 777643-01
DMI4000 B Fluorescence Microscope	Leica	https://www.leica-microsystems.com/products/light-microscopes/p/leica-dmi4000-b/
Vt1200 Semiautomatic vibrating blade microtome	Leica	https://www.leicabiosystems.com/histology-equipment/sliding-and-vibrating-blade-microtomes/vibrating-blade-microtomes/leica-vt1200/
BX61WI Upright microscope	Olympus	https://www.olympus-lifescience.com/en/microscopes/upright/bx61wi/
DMZ Universal Puller	Zeitz	https://www.zeitz-puller.com/
Multiclamp 700A/B Amplifiers	Science Products	https://science-products.com/en/shop/23/9/amplifiers-etc/amplifiers/patchclamp_amplifier/axon-multiclamp-700b
Axon Digidata 1550B data acquisition system	Molecular Devices	https://www.moleculardevices.com/products/axon-patch-clamp-system/digitizers/axon-digidata-1550b-plus-humsilencer#gref
Borosillicate glass capillaries	Harvard Apparatus	Cat# W330-0057
CoolLED pE-300	CoolLED	https://www.coolled.com/
ISO-Flex Stimulus Isolator	A.M.P.I.	http://www.ampi.co.il/isoflex.html
CSU22 Spinning Disk Microscope	Yokogawa	https://www.yokogawa.com/de/solutions/discontinued/csu22/
488nm Laser	Coherent	https://www.coherent.com/lasers/main/sapphire-lasers
Ixon DU-897D CCD	Andor	http://occult.mit.edu/instrumentation/MORIS/Documents/DU-897_BI.pdf

RESOURCE AVAILABILITY

Lead Contact

Further information and requests related to this study should be directed to and will be fulfilled by the lead contact, Prateep Beed (prateep.beed@charite.de).

Materials Availability

This study did not generate new unique reagents.

Data and Code Availability

The datasets and code supporting related to this study can be found on online repositories (see Key Resources Table), or upon request to the lead author. Original data have been deposited to Figshare: https://doi.org/10.6084/m9.figshare.13154321.v1.

EXPERIMENTAL MODEL AND SUBJECT DETAILS

All *in vivo* experiments were conducted according to regulations of the Berlin Landesamt für Gesundheit und Soziales (G0150/17). All animal maintenance for *in vitro* experiments was performed in accordance with Berlin Landesamt für Gesundheit und Soziales (Berlin T 0100/03).

For the first portion of this study (Figure 1), adult C57Bl6/n mice of both sexes were used. For subsequent experiments, L3-specific Oxr1-Cre mice (https://www.jax.org/strain/030484, Suh et al., 2011) were crossed with Ai40D mice (https://www.jax.org/strain/021188) or Ai32 mice (https://www.jax.org/strain/012569, Madisen et al., 2015) for selective expression of archaeorhodopsin or

channelrhodopsin, respectively. Uchl1-Cre mice were obtained from the Mutant Mouse Regional Resource Center. (MMRC, USA, Fuchs et al., 2016). For calcium imaging experiments, Nex-Cre mice (Goebbels et al., 2006) were crossed with Ai95 animals (https://www.jax.org/strain/024105; Madisen et al., 2015) for constitutive GCaMP6f expression in pyramidal cells only. Naive offspring of both sexes for all lines were used. Analyses of the influence of sex in our results were not performed due to small sample sizes. Adult mice (p > 30) were used for *in vivo* experiments (Figures 3 and S4), whereas brain slices for *in vitro* experiments were obtained from mice p12–18 (Figures 1, 2, 4, 5, S1, S2, and S3) and p12–28 (Figures 3 and S5). All animals were housed with a 12-hour light/dark cycle in group cages, with *ad libitum* access to water and standard rodent chow.

METHOD DETAILS

Surgery

For viral injections, mice were deeply anaesthetized with 2% isofluorane and a craniotomy was performed, exposing the transverse sinus 3.3ML from the midline. An injection needle was slowly lowered 0.3mm anterior to the edge of the sinus at an angle of −8° in the antero-posterior axis to a depth of 1.8DV using a micromanipulator. 500nl of pAAV-Ef1a-DIO eNpHR 3.0-EYFP (a gift from Karl Deisseroth; Addgene viral prep # 26966-AAV1) was injected at a speed of 50nl/min (Neurostar, Tübingen, Germany), waiting several minutes before withdrawing the needle. Mice were provided with carprofen and metamizol and left to recover for one month in their home cages before acute recordings.

For acute recordings, mice were deeply anaesthetized by intraperitoneal injection of a 10% urethane solution (1-1.5g/kg, Sigma Aldrich, Munich Germany). A craniotomy was performed above the MEC based on coordinates from the Paxinos and Franklin Brain Atlas (2001) at approximately ± 3.3ML and 0.5 anterior to lambda.

32-channel linear silicone probes or optrodes (NeuroNexus, Ann Arbor MI) were painted with the fluorescent dye DiI (Thermo Fisher Scientific, Schwerte Germany) and lowered slowly into the craniotomy at a 20° angle in the sagittal plane using a micromanipulator. An Ag/AgCl ground wire was placed into a well with saline anterior to the recording site. Signals were sampled at 20KHz with an RHD2000 amplifier (Intan Technologies, Los Angeles, California), and visualized using on-board recording software. Recordings began after a minimum 10 min waiting period at a depth at which clear up states could consistently be seen at a frequency of approximately 0.1Hz. During recordings, body temperature was maintained at 36° using a heating pad.

In Vivo Recordings

For optogenetic pulse barrage experiments, a 10 min baseline was first recorded. Then, a 10Hz light ON protocol (for 5 s) was applied using a 525nm PlexBright LED (Plexon, Dallas TX) coupled directly to the silicon optrode. This was repeated after a 5 s light OFF period. These dual barrages were repeated every 10 s over 20 min.

A closed-loop optogenetic stimulation system was created by routing one channel of the LFP via a National Instruments BNC-2110 shielded connector block (National Instruments, Austin TX) to a computer running Simulink (Mathworks, Natick NJ). Whenever a threshold detecting event was detected, a pulse was emitted to the LED, with a delay of approximately 50ms (data not shown).

After recordings were completed, mice were given a further urethane overdose, then perfused transcardially with 0.1M PBS followed by 4% paraformaldehyde. Brains were kept in PFA overnight, then sliced using a vibratome (Leica Microsystems, Wetzlar Germany) into 100μM sagittal slices and mounted for post hoc anatomical identification of recording sites and immunohistochemical stainings (see 'Histological Procedure', below). Images of probe tracks and stainings were obtained using a Leica DMI 4000B fluorescence microscope (Leica, Wetzlar, Germany). Only recordings with clear probe tracks in superficial layers of the MEC were used for subsequent analysis.

Analysis of *In Vivo* Data

All analysis was performed using custom scripts written in MATLAB (Mathworks, Natick NJ). For each recording, a sample channel was taken from the tip of the silicon probe in L3, and down-sampled from 20 to 0.2 kHz. Up states were detected using a modified version of the MAUDs algorithm (Seamari et al., 2007). Briefly, the LFP was filtered between 1 and 4 Hz, and smoothed using a Savitzky-Golay filter. Deflections two standard deviations above the median were calculated with a moving window, and compared with periods of elevated multiunit activity extracted with Kilosort2 (Pachitariu et al., 2016) to find indices of up states. From these indices, the spectral content of these up states could be calculated with the Stockwell Transform (Stockwell et al., 1996), as well as information about their duration and frequency.

The effect of LED pulse barrages was calculated by detecting the number of up states occurring inside of stimulation epochs, and comparing it to the same number of light OFF epochs of equivalent length (i.e., 50ms) randomly sampled from the rest of the recording.

The effect of closed loop stimulation was measured by comparing the properties of up states detected in a 10 min baseline and 10 min period of stimulation.

In vitro Slice Preparation

Near horizontal slices (~15° off the horizontal plane) of the medial entorhinal cortex (MEC) were obtained from C57Bl6/n mice. Animals were anesthetized with isofluorane and decapitated. The brains were quickly removed and placed in ice-cold (~4°C) artificial cerebrospinal fluid (ACSF) (pH 7.4) containing (in mM) 85 NaCl, 25 NaHCO3, 75 Sucrose, 10 Glucose, 2.5 KCl, 1.25 NaH2PO4,

3.5MgSO4, 0.5 CaCl2, and aerated with 95% O2, 5% CO2. Tissue blocks containing the brain region of interest were mounted on a vibratome (Leica VT 1200, Leica Microsystems), cut at 400 μm thickness, and incubated at 35°C for 30 min. In the case of mini-slices a needle (diameter = 0.60 mm) was used to dissect the MEC from the LEC and the hippocampus proper. The slices were then transferred to ACSF containing (in mM) 85 NaCl, 25 NaHCO3, 75 Sucrose, 10 Glucose, 2.5 KCl, 1.25 NaH2PO4, 3.5 MgSO4, 0.5 CaCl2. The slices were stored at room temperature in a submerged chamber for 1–5 hr before being transferred to the recording chamber.

In Vitro Electrophyisiology

For recordings, a slice was transferred to a submersion style recording chamber located on the stage of an upright, fixed-stage microscope (BX51WI, Olympus, Hamburg Germany) equipped with a water immersion objective and a near-infrared charge-coupled device (CCD) camera. The slices were perfused with ACSF (~35°C bubbled with 95% O2%–5% CO2) at 3–5 m/min to maintain neuronal health throughout the slice. The ACSF had the same composition as the incubation solution except for the concentrations of calcium and magnesium, which were reduced to 1.2 and 1.0 mM, respectively. Recording electrodes with impedance of 3–5 MOhm were pulled from borosilicate glass capillaries (Harvard Apparatus, Kent, UK; 1.5 mm OD) using a micropipette electrode puller (DMZ Universal Puller, Zeitz, Martinsried Germany). The intracellular solution contained the following (in mM): 135 K-gluconate, 6 KCl, 2 MgCl2, 0.2 EGTA, 5 Na2-phosphocreatine, 2 Na2-ATP, 0.5 Na2-GTP, 10 HEPES buffer, and 0.2% biocytin. The pH was adjusted to 7.2 with KOH. Recordings were performed using Multiclamp 700A/B amplifiers (Science Products, Hofheim Germany). The seal resistance was >1 GΩ. Capacitance compensation was maximal and bridge balance adjusted. Signals were filtered at 6 kHz, sampled at 20 kHz, and digitized using the Digidata 1550 and pClamp 10 (Molecular Devices, San Jose, CA, USA).

Stimulation experiments were performed using a bipolar micro-electrode (glass pipet filled with ACSF solution, wrapped by a fine grounding wire). A 4x objective was used to visually guide the stimulating electrode into the MEC. The inter-stimulus interval was ten seconds with a duration of 50 μs for each stimulus, using an isolated voltage stimulator (ISO-Flex, A.M.P.I., Israel).

In vitro GABA uncaging was done by a blue light LED (CoolLED pE-300 system with 470nm light) which photolysed the caged Rubi-GABA (Tocris, UK). When a spike was detected on an upstate, 500ms of blue light was used to uncage Rubi-GABA. *In vitro* optogenetic stimulation was done using a green light LED for stimulation of ArchT positive cells. For current and voltage clamp recordings of ArchT mediated hyperpolarization we used a 500ms light pulse. For suppression of spikes we used 50ms light pulse at 19Hz for 2 s.

Calcium Imaging

For population Ca^{2+} imaging of neonatal spontaneous synchronous network events, the genetically encoded Ca^{2+} indicator (GECI) GCaMP6f was used. Ca^{2+} imaging was performed using a Yokogawa CSU-22 spinning disc microscope (Yokogawa, Wehr, Germany) at 5000rpm. The spinning disc confocal permitted the generation of a large field of view time series at a high acquisition rate. A 488nm laser (Coherent, Santa Clara, CA, USA) was focused onto the field of view using a 4x, 40x or 60x objective. Emission light was filtered using a 515 ± 15nm bandpass filter. Fluorescence was detected using an Andor Ixon DU-897D back-illuminated CCD (Andor, Belfast, UK), with a pixel size of 16μm. Andor iQ software was used for data acquisition.

For data analysis, we used the SAMUROI python package (Rueckl et al., 2017) in combination with custom python routines. Events were detected using a template matching based algorithm, the onset was determined as the time point in an event when the signal reached two standard deviations above the mean standard deviation of the baseline. Signal onsets were used for synchrony analysis.

Histological Procedure

At the end of the recording session, the electrode was carefully detached from the recorded cell and the slice was fixed with 4% paraformaldehyde in 0.1 M phosphate buffer (PB) for at least 24 h at 4°C, then washed three times in 0.1 M PBS. Slices were then incubated in PBS containing 1% Triton X-100 and 5% normal goat serum for 4 hr at room temperature (RT). To visualize biocytin-filled cells we used Streptavidin Alexa 488/ 555 conjugate (S32354/S21381, 1:500, Invitrogen). CTIP2 (1:500 Rat, Abcam, Cambridge, UK) was used to visualize L5b, WFS1 (1:1000, Rabbit, Proteintech, IL, USA) to visualize L2 border with L3 as it stains for L2 pyramids in the MEC, antiGFP (ab18465, 1:1000, Chicken, Abcam, Cambridge, UK) for visualizing the expression of Arch in the Oxr1-Cre x Ai40D mice, and NeuN for visualizing neuronal cell bodies (ABN90, 1:1000, Guinea Pig, Millipore, Darmstadt Germany). Slices were incubated with primary antibodies for 48 hr at RT. After rinsing two times in PBS, sections were incubated in the PBS solution containing 0.5% Triton X-100, and Streptavidin Alexa 488/ 555 conjugate (for biocytin-filled neurons, S32354/ s21381, Invitrogen Corporation, Carlsbad, CA) or goat anti-rat conjugated with Alexa fluor 555 (for CTIP2, A-21434, 1:500 Invitrogen Corporation, Carlsbad, CA) or goat anti-guinea pig Alexa fluor 405 (for NeuN, ab175678, Abcam, Cambridge UK). Slices were mounted in Mowiol (Sigma Aldrich, Darmstadt Germany) under coverslips 2-3 hr after incubation with the secondary antibodies and stored at 4°C. Labeled cells were visualized using 20x or 40x objectives on a confocal microscope system (Leica, Wetzlar Germany). Z stack projections were optimized to examine the full extent of somato-dendritic compartments and axonal arborization. Image stacks obtained were registered and combined in Fiji (Schindelin et al., 2012) to form a montage of the sections.

Analysis of *In Vitro* Data

Up state onset, frequency and duration *in vitro* were quantified by using a modified version of the MAUDS algorithm that was published in Seamari et al. (2007). Spike probability is defined as the ration of the number of up states with spikes to total number of up states, spike frequency is the total number of spikes divided by the whole recording time and spikes per up state denotes the number

of spikes elicited only during up states. Analyses were performed using custom scripts written in MATLAB (The MathWorks, Natick, MA), Microsoft Office Excel (Microsoft, Redmond, WA), and ImageJ (Schneider et al., 2012).

QUANTIFICATION AND STATISTICAL ANALYSES

No randomization or blinding was performed during the execution of experiments or data analysis for this paper. No statistical methods were used for predetermining sample sizes. Data are presented in figures as mean ± SEM unless otherwise stated. Statistical analyses were performed using MATLAB (The MathWorks, Natick, MA), and Graphpad Prism (La Jolla, CA, USA). For data violating assumptions of normality (determined via a Kolmogorov-Smirnov test), non-parametric tests were used. Reported p values were all based on tests mentioned in the text. Significance was accepted at $p < 0.05$ and labeled as: n.s. (non significant) for $p > 0.05$, $^{*}p < 0.05$ and $^{**}p < 0.01$.

Cell Reports, Volume *33*

Supplemental Information

Layer 3 Pyramidal Cells in the Medial Entorhinal Cortex Orchestrate Up-Down States and Entrain the Deep Layers Differentially

Prateep Beed, Roberto de Filippo, Constance Holman, Friedrich W. Johenning, Christian Leibold, Antonio Caputi, Hannah Monyer, and Dietmar Schmitz

Supplemental Information

Layer 3 pyramidal cells in the medial entorhinal cortex orchestrate up-down states and entrain the deep layers differentially

Prateep Beed, Roberto de Filippo, Constance Holman, Friedrich W. Johenning, Christian Leibold, Antonio Caputi, Hannah Monyer & Dietmar Schmitz

Inventory of Supplemental Information

The Supplemental Information contains the following items:

Supplementary Figures S1 - S5

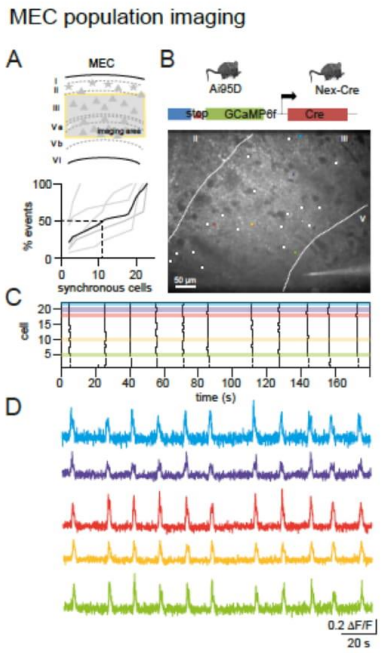

Figure S1 (related to Figure 1): Calcium imaging for synchronous activity.

(A) Top: *In vitro* calcium imaging was performed with a 20x objective over a field of view marked with the yellow box that included L3. Bottom: Cumulative distribution plot of the number of synchronous cells in all recorded events (n = 5 slices, 20-33 cells per slice). Grey lines are individual experiments and black line is the average.
(B) Top: Ai95D mice were crossbred with Nex-Cre animals for GCaMP6f expression in pyramidal cells only. Averaged fluorescence image of a time series. Markers in the fluorescence image correspond to analyzed cells.
(C) Raster plot of up state onsets of individual cells labelled in (B)
(D) Temporally aligned fluorescence traces of the color labeled cells in (B) and (C).

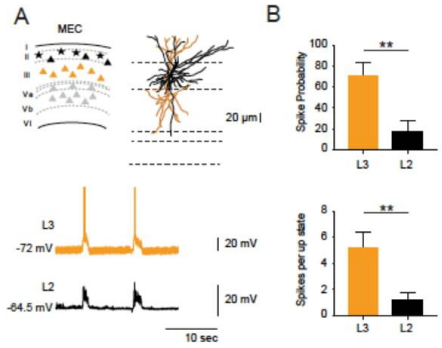

Figure S2 (related to Figure 1): L3 pyramidal cells are more active than L2 stellate cells during up down states.

(A) L3 pyramidal cells (in orange) were patched simultaneously with L2 stellate cells (in black). Upper trace is from the L3 pyramidal cell and lower trace is from the L2 stellate cell depicted in biocytin reconstructions.
(B) Upper panel: Spike probability (Up states with spikes / total number of up states) was significantly different between L3 and L2 cells. Lower panel: Spikes per up state was significantly higher in L3 pyramidal cells compared to L2 stellate cells (n = 9 cells for L3 and 10 cells for L2).

Data are presented as mean ± SEM

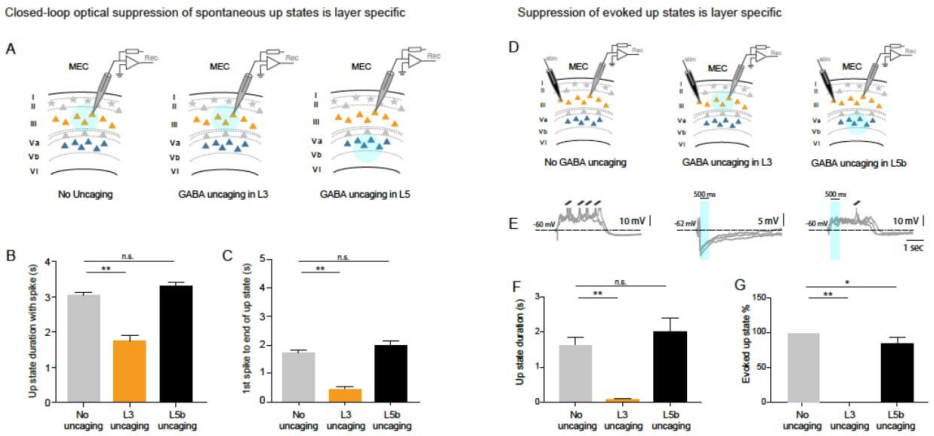

Figure S3 (related to Figure 2): Suppression of up states is layer specific in the MEC.

Hyperpolarizing L5 cells had no effect on up-down states (UDS) in the MEC in contrast to hyperpolarization of L3 cells, suggesting that suppression of UDS in the MEC is layer specific.
(A) Schematic of closed-loop GABA uncaging experiments for spontaneously occurring up states. As soon as an up state with spikes was detected, GABA was uncaged using LED-emitted blue light (488 nm) for 500ms either in L3 (middle panel) or L5 (right panel). No uncaging served as control (left panel).
(B) Duration of up states was reduced when GABA was uncaged in L3 (n = 41 up states from 5 cells), while GABA uncaging in L5 (n = 47 up states from 5 cells) had no effect compared to no uncaging control (n = 84 up states from 5 cells).
(C) Time from 1st spike (when GABA was uncaged) to the end of up state was reduced upon GABA uncaging in L3 (n = 41 up states from 5 cells), while GABA uncaging in L5 (n = 47 up states from 5 cells) had no effect compared to no uncaging control (n = 84 up states from 5 cells).
(D) Schematic of GABA uncaging experiments for evoked up states. 100ms after an evoked up state, GABA was uncaged for 500ms using blue light (488 nm) either in L3 (middle panel) or L5 (right panel) with no uncaging as control (left panel)
(E) Example traces for the 3 conditions above (action potentials are clipped).
(F) Duration of up states was reduced when GABA was uncaged in L3 (n = 20 up states from 4 cells), while GABA uncaging in L5 (n = 12 up states from 3 cells) had no effect compared to no uncaging control (n = 21 up states from 5 cells).
(G) Percentage of evoked up states were completely suppressed by GABA uncaging in L3 (n = 4 cells) while it had a mild suppression of evoked up states when GABA was uncaged in L5 (n = 3 cells) when compared to no uncaging control (n = 5 cells).

Data are presented as mean ± SEM

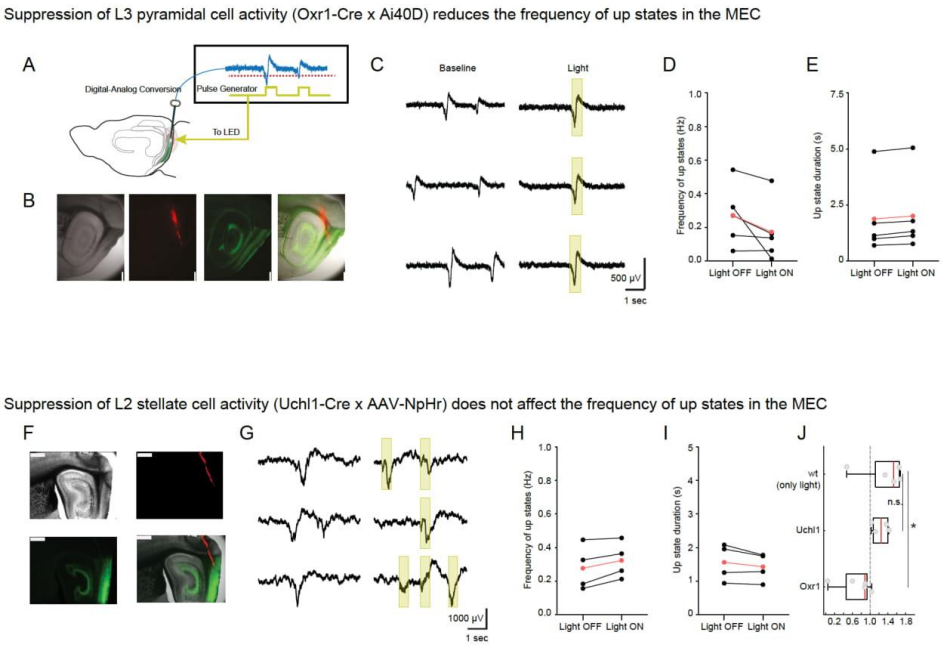

Figure S4 (related to Figure 3): Suppression of L3 pyramidal cell activity in L3 (Oxr1-Cre x Ai40D) reduces the frequency of up states in the MEC.

(A) Schematic showing activation of LED when LFP crosses threshold using a closed-loop system.
(B) Example sagittal section showing recording site in L3 of Oxr1-Cre x Ai40D mouse showing DiI trace from silicon probe (left), Oxr1+ ArchT expressing fibers (middle) and overlay (right). Scale bar = 500µm.
(C) Example traces showing 5 second excerpts from LFP in baseline (light OFF, left) and during stimulation period (light ON, right). Yellow rectangles show LED illumination during detected up states.
(D) Average up state frequency in 10 min light OFF and light ON periods in Oxr1-Cre x Ai40D mice (Hz). Black lines represent individual recordings, red line shows the group average (n = 5 recordings from 5 animals).
(E) Average up state duration in 10 min light OFF and light ON periods in Oxr1-Cre x Ai40D mice (ms). Black lines represent individual recordings, red line is the group average (n = 5 recordings from 5 animals).
(F) Example sagittal section showing recording site in L2 of Uchl1-Cre x AAV- eNpHR3.0-EGFP mouse showing DiI trace from silicon probe (right), halorhodopsin-expressing cells (lower left) and overlay (lower right). Scale bar = 750µm.
(G) Example traces showing 5-second excerpts from LFP in baseline (light OFF, left) and during stimulation period (light ON, right). Yellow rectangles show LED illumination during detected up states.
(H) Average up state frequency in 10 min light OFF and light ON periods in Uchl1-Cre x AAV- eNpHR3.0-EGFP mice (Hz). Black lines represent individual recordings; Red line is the group average (n = 4 recordings from 3 animals).
(I) Average upstate duration in 10 min light OFF and light ON periods in Uchl1-Cre x AAV- eNpHR3.0-EGFP mice (ms). Black lines represent individual recordings, red line is the group average (n = 4 recordings from 3 animals).
(J) Comparison of up state frequency normalized to baseline (light OFF periods) frequency in wildtype (top), Uchl1-Cre x AAV eNpHR3.0-EGFP (middle) and Oxr1-Cre x Ai40D mice (bottom). Red lines indicate the median of each group, box edges show 25th and 75th percentile, respectively. Whiskers extend to most extreme data points (n = 5, 4, and 5 recordings from 4, 3, and 5 animals, respectively).

Data are presented as mean ± SEM

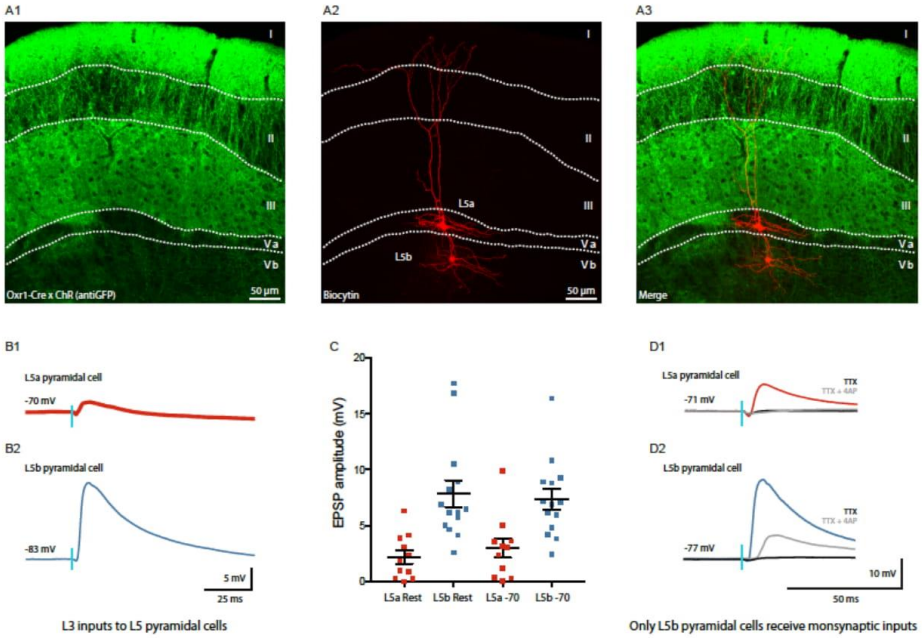

Figure S5 (related to Figure 5): Mapping L3 inputs to L5 pyramidal cells using the Oxr1-Cre x ChR mice.

(A1) Distribution of ChR expressing fibers from Oxr1 positive L3 pyramidal cells in the MEC.
(A2) L5a and L5b pyramidal cells filled with biocytin were recorded from and L3 inputs mapped onto them.
(A3) Merge of A1 and A2.
(B1) L3 input (2ms blue LED in current clamp) onto L5a pyramidal cell at resting membrane potential. An average of 10 traces is shown.
(B2) Same as in B1 but for L5b pyramidal cell.
(C) Overview of input amplitudes onto L5a (n = 11 cells) and L5b (n = 14 cells) pyramidal cells recorded at resting membrane potential and at -70mV.
(D1) Test of monosynaptic input onto L5a and in (D2) L5b pyramidal cell using the TTX-4AP approach. An average of 10 traces is shown. L5b pyramidal cells receive monosynaptic input from L3 Oxr1 positive pyramidal cells.

Data are presented as mean ± SEM

14. Curriculum Vitae:

My curriculum vitae does not appear in the electronic version of my paper for reasons of data protection.

15. Complete Publication List:

Beed, P.*, De Fillippo R*, **Holman C.***, Johenning F.W., Leibold C, Caputi, A., Monyer, H., Schmitz D. Layer 3 pyramidal cells in the medial entorhinal cortex orchestrate Up-down states and entrain the deep layers differentially. Cell Reports *33*, 2020, https://doi.org/10.1016/j.celrep.2020.108470
IF (2019) = 8.109

Aberrant gamma oscillations in rat prefrontal cortex and hippocampus after single application of MK-801. Lermercier C, **Holman C**, Gerevich Z. Schizophrenia Research, 2017, pii: S0920-9964(17)30014-2. doi: 10.1016/j.schres.2017.01.017.
IF (2019) = 4.56

Where have all the rodents gone? The effects of attrition in preclinical research in stroke and cancer.
Holman C, Piper S, Grittner U, Diamantaras A, Siegerink B, Kimmelman J, Dirnagl U. PloS Biology, 2016 14(1): e1002331. doi:10.1371/journal.pbio.1002331.
IF (2019) = 7.076

Theta oscillations regulate the speed of locomotion via a hippocampus to lateral septum pathway. Bender, F., Gorbati, M., Carus M., Denisova, N., Gao X., **Holman, C**., Korotkova, T., Ponomarenko A. Nature Communications, October 2015, doi:10.1038/ncomms9521
IF (2019) = 12.121

Indestructible plastic: Exploring new avenues of change in the aging brain
Holman, C., and De Villers-Sidani, E. Frontiers in Human Neuroscience, April 2014. doi: 10.3389/fnhum.2014.00219
IF (2019) = 3.209

Shaping the aging brain: role of auditory input patterns in the emergence of auditory cortical impairments. Kamal, B., **Holman, C**. and De Villers-Sidani, E. Frontiers in Systems Neuroscience September 2013. doi: 10.3389/fnsys.2013.00052
IF (2019) = 3.293

16. Acknowledgements

First and foremost, I would like to thank Dietmar Schmitz for giving me the opportunity to perform my master's and PhD work in his lab, as well as supporting me in career development. I am also deeply indebted my supervisor, John Tukker, for his help, insights, generosity and kindness over the past 6 years. I would also like to extend a special thanks to the other members of my thesis committee, Richard Kempter and Michael Brecht for their support and suggestions for my projects.

The work in this thesis would not have been possible without contributions of many other great scientists. First, I would like to share my gratitude to Eric Reifenstein for his help with phase precession analysis, and constant willingness to engage in discussion and answer questions. I would also like to highlight the contributions of Jean Simonnet, who proved invaluable in setting up spatial coding analysis. I am also especially grateful for my co-authors on the up down state paper, particularly Prateep Beed and Roberto de Filippo. It was a pleasure to work as part of a team with them. I would also like to thank the Moser lab for their hospitality especially Ingvild Ulsaker-Janke and Nenitha Dagslott for their help in sharing chronic implant protocols. I would also like to thank Anke Schönherr, Susanne Rieckmann and Katja Czieselsky for their excellent technical assistance in Berlin. This work would absolutely also not have been possible with support of colleagues at the QUEST Center, including my supervisor Tracey Weissgerber.

I am also very thankful to the many brilliant people who provided helpful feedback on earlier drafts of this thesis, including John, Eric, Prateep, Daniel Parthier and Stephen Lenzi. I would also like to thank Prateep, Daniel and Alexander Stumpf for their help with *in vitro* testing of viral constructs used in this study. This thanks indeed goes out to all members of the Schmitz Lab past and present for creating a wonderful working environment. I will miss all of you.

Finally, I am incredibly grateful to my family and partner, Gregor, for being a constant source of support and comfort for my years in the lab. From day-to-day to global pandemic, I know that I can always depend on you.

Thank you.

Berlin, April 2021.